Columnar cholinergic neurotransmission onto T5 cells of *Drosophila*

Eleni Samara[1,2*], Tabea Schilling[1], Inês M. A. Ribeiro[1,3], Juergen Haag[1], Maria-Bianca Leonte[1,2], Alexander Borst[1,4*]

[1] Max Planck Institute for Biological Intelligence, Department of Circuits-Computation-Models, 82152 Planegg, Germany

[2] Graduate School of Systemic Neurosciences, LMU Munich, 82152 Planegg, Germany

[3] Institute of Medical Psychology, Medical Faculty, LMU Munich, 80336 Munich, Germany

[4] Lead contact

*Correspondence: eleni.samara@bi.mpg.de (E.S.), alexander.borst@bi.mpg.de (A.B.)

Summary

A large variety of acetylcholine receptors (AChRs), nicotinic and muscarinic, are expressed in the brain of *Drosophila melanogaster*. Nonetheless, how AChRs affect brain function remains poorly understood. T5 cells are the primary motion-sensing neurons in the OFF-motion pathway and receive visual input from four different columnar cholinergic neurons, Tm1, Tm2, Tm4 and Tm9. We reasoned that different postsynaptic AChRs might also contribute to T5 function. We demonstrate that the nicotinic nAChRα1, nAChRα4, nAChRα5 and nAChRα7 subunits localize on T5 dendrites. By targeting synaptic markers specifically to each cholinergic input neuron, we uncover a prevalence of the nAChRα5 in Tm1, Tm2 and Tm4 synapses and of nAChRα7 in Tm9 synapses on T5 dendrites. Knock-down of nAChRα4, nAChRα5, nAChRα7, and mAChR-B individually alters the optomotor response and reduces T5 directional selectivity. Our findings expose the complex molecular mechanisms underlying motion detection in T5 cells and offer a system to study AChRs in visual information processing.

Introduction

Neurotransmission is a key process of neuronal communication that entails the release of neurotransmitter from the presynaptic terminal and its binding by

receptors on the postsynaptic membrane. In *Drosophila melanogaster*, the neurotransmitters acetylcholine, GABA, glutamate, dopamine, serotonin, octopamine[1] and histamine[2] are used for various neuronal tasks. Amongst them, the prime excitatory neurotransmitter is acetylcholine[3,4,5], which can bind to a large number of structurally diverse acetylcholine receptors (AChRs)[6,7,8,9]. How this structural variety supports specific neural computations is not understood.

AChRs comprise two categories in bilaterians and cnidarians[10]: the fast ionotropic nicotinic receptors (nAChRs) and the slow metabotropic muscarinic receptors (mAChRs). nAChRs are activated by acetylcholine (ACh) and the agonist nicotine and belong to the cys-loop ligand-gated ion channel superfamily, forming functional pentamers of various subunit stoichiometries, homomeric or heteromeric. In *Drosophila*, the pentameric nAChR formation is achieved from a pool of seven α and three β subunits[11,12,13]. mAChRs are activated by ACh and the agonist muscarine and are G protein-coupled receptors (GPCRs), comprising three types, A, B and C in *Drosophila*[14,15,16]. These mAChR types activate different signaling cascades, with the mAChR-A and mAChR-C being coupled to the $G_{q/11}$ signaling cascade and the mAChR-B to the $G_{i/0}$[15,17,18]. Although the variety of AChRs has been thoroughly addressed at the biochemical level[18,19], our understanding at the circuit level in terms of neural computations and their behavioral output is still at the beginning[14,20,21,22,23,].

Among sensory modalities, vision contributes the most synaptic input to the *Drosophila* central brain[24]. Visual processing starts at the two compound eyes, whose retinotopic organization leads to a repetitive circuitry across its ~ 850 facets[25,26]. The major neuroanatomical area in the fly's brain for visual information processing is the optic lobe, which is divided in four neuropils, the lamina, the medulla, the lobula and the lobula plate. From the different visual cues such as color and polarization vision[27], motion vision has been thoroughly investigated, mainly due to its importance in the survival and navigation of the individual[28,29]. The photoreceptor-derived information is split into two pathways: the ON-pathway for luminance increments and the OFF-pathway for luminance decrements[30,31]. Along the motion vision circuitry, the first neurons that compute directional information are T4 cells in the ON-pathway and T5 cells in the OFF-pathway[32,33].

Both T4 and T5 cells share the same bifurcation principles, with the dendrite giving rise to the axonal terminal fiber and to the soma fiber[34]. The T4 dendrites are located in medulla layer ten (M10) and the T5 dendrites in lobula layer one (LO1). T4 and T5 cells exist in four subtypes per column: a, b, c and d. Each subtype has its dendrite oriented in one of the four cardinal directions and responds to front-to-back, back-to-front, upward or downward motion, respectively[33,34,35,36]. Furthermore, each subtype has its axonal terminals in one of the four layers in lobula plate[34]. For their directional responses, T4 and T5 cells rely on the visual information they receive from input neurons. The major upstream columnar neurons of T4 cells are the excitatory cholinergic Mi1 and Tm3 neurons, the glutamatergic Mi9 and the inhibitory GABAergic CT1, C3 and Mi4 neurons[37,38,39,40,41,42,43,44]. For T5 cells, the main columnar input neurons are the excitatory cholinergic Tm1, Tm2, Tm4 and Tm9 cells and the inhibitory GABAergic CT1 neuron[39,41,42,43,45,46,47,48,49]. T4 and T5 cells collect their inputs in a distinct spatial order[39] reflecting their specific directional tuning[50,51].

T4 and T5 cells achieve their response selectivity for a particular direction by a combination of two mechanisms: preferred direction enhancement and null direction suppression[51,52]. In both processes, the luminance signal from one point in visual space is delayed and interacts with the instantaneous signal from a neighboring visual point. For preferred direction enhancement, the delayed signal is from the preferred side of the cell, i.e. where a stimulus moving in the preferred direction enters the receptive field of the cell, and amplifies the central signal. For null direction suppression, the delayed signal is from the opposite, the so-called null side, and is used to suppress the central signal. In T4 cells, the preferred direction enhancement is biophysically implemented by a release from shunting inhibition, mediated by the glutamatergic, inhibitory OFF-center cell Mi9, which amplifies the central excitatory input from Mi1 and Tm3 neurons[44]. For the null direction suppression, the inhibitory neurons CT1, Mi4 and C3 act in concert to inhibit the Mi1-Tm3 signal. In T5 cells, the CT1 cell is responsible for null direction suppression[49]. It is, however, unclear how the different cholinergic inputs accomplish a preferred direction enhancement. While the functional consequences of the different T5 input neurons have been addressed in the past[46,53], the functional implications of a possible input-specific AChR composition on T5 dendrites have not been considered.

In this study, we address the structural and functional variety of different AChRs in T5 cells. We first show that the nAChRα1, nAChRα4, nAChRα5 and nAChRα7 subunits localize on T5 dendrites. Using cell-specific synaptic markers for the different columnar cholinergic inputs, we find a prevalence of the nAChRα5 subunit in Tm1, Tm2 and Tm4 synapses and the nAChRα7 subunit enrichment in Tm9 synapses**.** Through a combinatorial approach of neuronal input spatial wiring and synaptic receptor mapping, we demonstrate the complex columnar cholinergic spatial wiring on T5 dendrites. Finally, we show that the nAChRα4, nAChRα5 and nAChRα7 subunits, as well as the mAChR-B type, differentially contribute to the optomotor response and to the directional responses of T5 cells.

Results

Expression of AChRs in T5 cells

Information about the expression of AChRs in T5 cells is available at the RNA level[42,54,55], but is lacking at the protein level. We first evaluated the endogenous expression of the nAChRα1, nAChRα2, nAChRα4, nAChRα5, nAChRα6 and nAChRα7 subunits on T5 dendrites (Figure 1A,B). We used nAChRα subunits endogenously tagged with an enhanced version of the green fluorescent protein (EGFP) generated by Pribbenow et al.,[22] thus minimizing the mistargeting error that can occur with overexpression of the receptor and allowing for the assessment of protein expression levels. Due to their non-conditional tagging[56,57], the localization of nAChRs in T5 neurons was verified by co-localizing the receptor puncta with the tdTomato expressed in T5 dendrites. From this subunit screening, we found the nAChRα1, nAChRα4, nAChRα5, nAChRα6 and nAChRα7 subunits on T5 dendrites, while the nAChRα2 subunit was not detected (Figure 1C-I). To ensure that the lack of nAChRα2 expression was T5-specific, we confirmed its expression in other LO layers in the optic lobe (Figure S1A). By quantifying the T5 nAChRα subunit density in regions of interest (ROIs) in LO1, we observed the prevalence of the nAChRα5 subunit and the low co-localization levels of the nAChRα2 and the nAChRα6 subunits with T5 dendrites, which is in alignment with previous nAChRα RNA expression levels[42,54] (Figure 1J, Figure S1B-D). A recent study[56] also confirmed the T5 dendritic localization of the nAChRα3 and nAChRβ1 subunits, which together with

our nAChRα1, nAChRα4, nAChRα5, nAChRα6 and nAChRα7 subunit expression, emphasizes the large variety of nAChRs on T5 dendrites. Next, we sought to identify the nAChRα expression patterns in the T5 axonal terminals by searching for the co-localization of the receptor puncta with the membrane-bound tdTomato expressed in T5 terminals. Both T4 and T5 neuronal populations were targeted. Due to the lack of neuropile distinction between T4 and T5 axonal terminals, our results cannot be attributed explicitly to T5 cells. The nAChRα1, nAChRα5, nAChRα6 and nAChRα7 subunits were detected in T4-T5 axonal terminals, while the nAChRα2 and nAChRα4 were not (Figure S2A-G). Additionally, we observed the reduction of the nAChRα1, nAChRα5 and nAChRα7 subunits in LOP after a T4-T5 specific subunit knock-down, indicative of their T4-T5 axonal synaptic localization (Figure S2J, S3A,C,D).

To study the mAChR expression on T5 dendrites, we used a line expressing the mAChR-B type under control of UAS. We observed the overexpressed mAChR-B protein localizing exclusively on T5 dendrites (Figure 1K, S2H). The encountered dendritic T5 mAChR-B type targeting might be the outcome of ectopic expression leading to dendritic protein targeting. We reasoned that if mAChR-B was mistargeted to T5 dendrites, this mistargeting would be observed in other cells and that over-expression of mAChR-B with a pan-neuronal driver would result in the presence of ectopic mAChR-B in all the dendrites of neurons in the fly brain (Figure S2I). Instead, the mAChR-B type followed an enrichment in layer 10, where T4 dendrites reside, and in LO1, where T5 dendrites reside, while being absent from some medulla layers and LOP. Thus, the dendritic and axonal terminal protein expression patterns differ between ionotropic and metabotropic AChRs and even within the same AChR (Figure S2K).

To investigate the expression of those AChRs where we lacked endogenously tagged lines for, and to verify the expression profiles reported in Figure 1, we used enhancer-trap GAL4 lines[58] (Figure S4A-L). By comparing RNA sequencing datasets[42,54] with the enhancer trap and the endogenously tagged experiments here and in previous studies[56], we concluded that the nicotinic nAChRα1, nAChRα3, nAChRα4, nAChRα5, nAChRα7 and nAChRβ1 subunits as well as the muscarinic mAChR-A and mAChR-B types are expressed in T5 cells, while the nAChRα2, nAChRα6, nAChRβ2 and nAChRβ3 subunits exhibit low to null expression levels

(Figure S4M). We did not further address the mAChR-C due to the lack of endogenously tagged and enhancer-trap lines, transcriptomics information and studies supporting its low brain expression levels[14,20]. In summary, the dendritic and axonal protein localization patterns of ionotropic and metabotropic AChRs in T5 cells are diverse, complex, and can even differ for the same AChR subunit.

Morphological identification of cholinergic T5 input neurons and synapse visualization

The nAChRα1, nAChRα4, nAChRα5 and nAChRα7 subunits might contribute to the directional responses of T5 by being present in all cholinergic synapses linking Tm1, Tm2, Tm4 and Tm9 to T5 dendrites, or to a subset of these. To discern between these possibilities, we focused on the protein localization of nAChRα subunits in specific synaptic pairs. We first needed genetic access to the four T5 cholinergic neuronal inputs: Tm1, Tm2, Tm4 and Tm9. The morphology of these input neurons has been extensively studied via Golgi staining[34] and electron microscopy reconstructions[38,39,45,48,59,60,61]. We used this previously attained EM morphological knowledge to cross-validate our light microscopy screening of potential Tm-specific enhancer lines (Figure 2A,D,G,J). Both Gal4 and LexA driver lines[62,63] were tested and their efficacy was assessed in terms of neuronal specificity and whole population targeting. Neuronal specificity was evaluated based on the arborization pattern of each neuronal type and the LO layer where the axonal terminals are localized. To achieve sparse and stochastic neuronal labelling, we used the Multi-color FlpOut approach[64] and observed axonal terminals in LO layer 1 for Tm1 (Figure 2A), up to layer 2 for Tm2 (Figure 2D), up to layer 4 for Tm4 (Figure 2G), and in layer 1 for Tm9 (Figure 2J), as expected from previous studies[34,39]. To exclude the developmental bias introduced by the Multi-color FlpOut approach, as well as the non-neuronal targeting induced by the heat-shock-activated flipase (Figure 2G), we supplemented our single cell labelling with whole population labelling of the Tm-Gal4 lines (Figure 2B,E,H,K). This approach revealed that the Gal4 driver lines could account for specific and whole population targeting of Tm1, Tm2, Tm4 and Tm9 cells. For the respective LexA[63,65] driver lines, the whole Tm1 population was successfully targeted (Figure 2C), but after comparing the results with the analogous Gal4 driver line, dendritic ramifications in layer 4 that do not correspond to Tm1, were observed. For Tm2, Tm4 and Tm9 LexA lines, we encountered sparse neuronal labelling, indicating

that the driver lines could not target the whole neuronal population (Figure 2F,I,L). Based on this morphological screening, we chose the Gal4 driver lines for the Tm-T5 synapse visualization.

To visualize synapses between Tm1, Tm2, Tm4, Tm9 and T5 cells, we screened for the available reporter tools. We first tested transgenes for GFP membrane targeting, which resulted in the visualization of the whole axonal process (Figure S5A), including the extra- and peri-synaptic sites in addition to the presynaptic compartment. The truncated version of the presynaptic marker Brp, one of the major protein participants of the protein-dense T-bar[66,67], named Brp^{short} [68,69] was also tested (Figure S5B). This Brp^{short}::GFP line labelled only the presynaptic sites of all the Tm synapses, regardless of their activity, without labelling their postsynaptic sites. Next, we sought to explore methods of trans-synaptic labelling such as GFP Reconstitution Across Synaptic Partners (GRASP)[70], where the GFP_{1-10} fragment is targeted to the cell membrane of the presynaptic compartment, while the GFP_{11} fragment is targeted to the cell membrane of the postsynaptic compartment. The targeted GRASP (t-GRASP)[71] allowed to capture all synapses between Tm and T5 cells, regardless of their activity (Figure S5C). The presence of reconstituted GFP signal in the inner optic chiasm, likely due to the ectopic reconstitution in the Tm4-T5 synapses and the fact that the receptor subunits of interest were also tagged with EGFP, led us to exclude this genetic method. The final reporter tool was that of the activity GRASP (syb-GRASP)[72]. The reconstituted GFP signal was indicative of the given synaptic activity at the point of the dissection, as the GFP_{1-10} fragment is tethered to the vesicular protein synaptobrevin, thus resulting in the syb-GRASP reconstitution being sparser than the t-GRASP reconstitution (Figure S5D). This approach did not allow for a quantitative analysis and together with the lack of spectral distinction between the synaptic and the receptor signal, syb-GRASP was not chosen for our experiments. In conclusion, our reporter tool screening for synaptic labelling pointed to Brp^{short} as a suitable marker to evaluate the synaptic localization of the nAChRα receptor subunits.

To validate the synaptic specificity of Brp^{short}, we assessed two different, well described synapses: the cholinergic Tm3-T4 and the glutamatergic Mi9-T4 synapse (Figure S6A,B). Brp$^{short::mCherry}$ [73] successfully showed the expected lack of trans-

synaptic alignment with the GABAergic receptor Rdl in Tm3-T4 synapses (Figure S6A), while it revealed trans-synaptic alignment with the glutamatergic receptor GluClα[44] in Mi9-T4 synapses (Figure S6B). To confirm the synaptic localization of $Brp^{short::mStraw}$, a chimera that has the same truncated form of Brp as in $Brp^{short::mCherry}$ but was instead fused with mStrawberry by Owald et al.,[74], we used an antibody against the endogenous Brp having affinity to amino acids absent from the truncated Brp^{short} form (Figure S6C). This approach revealed the pre-synaptic alignment of the endogenous Brp (Anti-Brp) with the Tm1, Tm2, Tm4 and Tm9 boutons ($Brp^{short::mStraw}$). These results, together with previous studies[68], speak in favor of $Brp^{short::mStraw}$ as a valid pre-synaptic marker in our circuit of interest.

The nAChRα5 subunit synaptic localization differs among the four cholinergic inputs

With $Brp^{short::mStraw}$ as a presynaptic marker, we evaluated the localization of the most highly expressed subunits, nAChRα1, nAChRα4, nAChRα5 and nAChRα7, along the Tm-T5 synapses on T5 dendrites. We focused on the Tm1, Tm2, Tm4 and Tm9 synapses in LO1, the major cholinergic inputs to T5. The regions of interest that we have chosen were restricted to LO1 so as to include the Tm-T5 synaptic connections (Figure S7A). We found that the nAChRα1, nAChRα4, nAChRα5 and nAChRα7 subunits localize to Tm1, Tm2, Tm4 and Tm9 synapses in LO1 (Figure 3A-D, Figure S7B). However, the Tm synapses in LO1 might account for other output neurons apart from T5 cells. To circumvent this, we used the FlyWire connectome data explorer (Codex) for the full adult fly brain (FAFB) dataset[59,60,61] in order to find the output neurons of the Tm1, Tm2, Tm4 and Tm9 synapses in LO1. This analysis revealed T5 cells as the principal output neuronal type across all four Tm cell types in LO1 (Figure S8A). Therefore, the quantification of the nAChRα subunit synaptic localization in LO1 principally corresponded to Tm-T5 synapses. Importantly, we found that not all Tm input neurons had the same synaptic receptor profiles. Tm1, Tm2 and Tm4-to-T5 synapses primarily used the nAChRα5 subunit, whereas Tm9-to-T5 mainly used the nAChRα7 subunit (Figure 3E-H). As the GABAergic neuron CT1 was a considerable Tm9 output in terms of synapse number (Figure S8A) we wondered if the Tm9-nAChRα7 subunit trans-synaptic alignment (Figure 3H) could be attributed to Tm9-T5 synapses as well. We generated new flies to employ a C-RASP approach. C-RASP follows the activity GRASP principles, but

instead of a GFP_{1-10} fragment uses a CFP_{1-10} fragment. This method showed the nAChRα7 subunit localization in Tm9-T5 synapses (Figure S8B).

Whether Tm1, Tm2, Tm4 and Tm9 cells differentiate from one another by differentially using muscarinic receptors as well, is currently unknown. We focused on the mAChR-B localization in Tm9-T5 synapses (Figure S9A). Overexpression of mAChR-B shows its localization to Tm9-T5 synapses, which is further supported by its localization pattern compared to the nAChRα5 subunit (Figure S9B). The apparent lack of a generalized cellular mistargeting of the mAChR-B overexpression line (Figure S2I), does not exclude the existence of synaptic mistargeting events. Consequently, our positive Tm9-mAChR-B results are indicative rather than definitive. Overall, our nAChRα subunit mapping across Tm synapses in LO1 revealed that Tm1, Tm2 and Tm4 cells differ from Tm9 at the postsynaptic level as well[46,53].

Spatial organization of Tm-nAChRα synapses in T5 dendrites

The compartmentalization of inputs and subsequently of receptors on T5 dendrites is essential for the T5 direction-selectivity[50,51,56,57]. Thus far, receptor localization in Tm-to-T5 synapses has been addressed by combining single-cell receptor localization and neuronal input spatial wiring information[56,57]. To advance this, we analyzed both T5a and T5c dendrites as representatives of the two directional systems from the FAFB[59] dataset via the FlyWire (flywire.ai)[60,61] interface. Manual proofreading of predicted synapses[75,76] revealed the strongest wiring in terms of synapse number of Tm9 compared to Tm1, Tm2 and Tm4, in both T5 subtypes as previously reported[39,49] (Figure 4A,B). These differences in synapse counts among the Tm inputs was the principal reason for measuring the synapse occupancy index, rather than mere co-localization events for the synaptic subunit mapping (Figure 3E-H). Next, we sought to identify the spatial wiring of the four Tm neurons in T5 dendrites. Our analysis revealed the Tm1, Tm2, Tm4 and Tm9 wiring at the central dendritic compartment, while Tm9 extended to the distal compartment as well, similarly to previous studies[39,49] (Figure 4C,D). In combination with our previous results, we concluded that the nAChRα1, nAChRα4 and nAChRα7 subunits localize across the dendrite in Tm1, Tm2, Tm4 and Tm9-T5 synapses, while the nAChRα5 subunit

localizes primarily in Tm1, Tm2 and Tm4-T5 synapses in the central dendritic compartment (Figure 4E).

AChRs differentially affect the optomotor response

When stimulated by rotatory visual motion, flies perform corrective steering maneuvers in their flight or walking trajectories. This behavior is called the optomotor response[77,78,79] and T4 and T5 cells are indispensable for its manifestation[80,81,82,83]. Therefore, molecular alterations that are crucial for the proper T5 function should be reflected in the fly's optomotor response behavior. We used reversed genetics to test the role of AChRs in the OFF-motion pathway. We knocked-down the expression of the nAChRα1, nAChRα4, nAChRα5 or nAChRα7 subunits as well as the mAChR-B type, and evaluated the optomotor response on the 'fly-on-ball' set up. To confirm the RNAi-induced reduction in AChR expression, we performed immunohistochemistry, where the RNAi effect was evaluated (Figure S3A-F). Given that each receptor has a unique developmental onset of expression (Figure S1D), we raised flies in 29°C[84,85] and used a T4-T5 driver line that was active from the third larval stage onwards[80,86] in order to achieve a strong protein expression knock-down. The driver line targeted all T5 subtypes and allowed for the RNAi induction prior to the peak of AChR expression (Figure S3G,H).

Flies walking on an air-suspended ball were exposed to a set of OFF edges moving in sixteen directions, which elicit a typical profile of angular walking velocities, with the highest amplitudes to horizontal motion and lowest amplitudes to vertical motion[44] (Figure 5A). Knock-down of the nAChRα1 subunit did not alter the angular velocity response profile to the OFF edges (Figure 5B,G). Knock-down of the nAChRα4 subunit and the mAChR-B type resulted in an increase of the angular velocity in response to OFF edges moving in both horizontal directions (Figure 5C,F,G). In contrast, knock-down of the nAChRα5 and the nAChRα7 subunits led to a decrease in the angular velocity amplitude in response to horizontal moving edges (Figure 5D,E,G). We have also addressed the nAChRα3 and nAChRβ1 subunits and the mAChR-A type. The nAChRα3 and nAChRβ1 subunits were recently found on T5 dendrites[56], whilst the mAChR-A type exhibited high RNA expression levels[42,54] as well as expression in T4-T5 cells (Figure S1C,D, S4K). Knock-down of nAChRα3, nAChRβ1 and mAChR-A did not affect the angular velocity of the flies in response to

OFF edges (Figure S10A-E). The RNAi efficiency against the nAChRα3 and nAChRβ1 subunits and the mAChR-A type could not be verified. These AChRs should therefore not be excluded from playing an important role in the optomotor response. In summary, we discovered that AChRs play different roles in the optomotor response.

Directional tuning of T5 cells changes after AChR knock-down

The nAChRα5 and nAChRα7 subunits localize both in T5 dendrites and in T5 axonal terminals (Figure S2K). The effects on the behavioral responses to OFF-edge horizontal motion that were observed upon nAChRα5 and nAChRα7 knock-down (Figure 5D,E,G) could either be due to functional roles in T5 dendrites or to T5 axonal terminals. To discern between these two possibilities, we measured calcium responses in T5 axonal terminals. We performed two-photon calcium imaging in T5c neurons, which are sensitive to upward motion as the preferred motion direction[33]. nAChRα4, nAChRα5, nAChRα7 or mAChR-B knock-down flies were stimulated by dark edges moving in sixteen different directions, while calcium responses were monitored in T5c axonal terminals in layer 3 of LOP (LOP3) (Figure 6A, Figure S11A-C). As in the behavioral experiments, RNA interference was induced prior to peak receptor expression with the use of a T4-T5 promoter that is active from the third larval stage[86], and raising flies in 29°C[84,85]. Knock-down of the nAChRα4 subunit led to a slight increase in calcium responses in response to the non-preferred (270°) direction (Figure 6B). Similarly, knock-down of the nAChRα5 subunit resulted in higher calcium responses to the edge moving in the non-preferred direction (Figure 6C), suggesting nAChRα5, and to a lesser extent, nAChRα4 contribute to directional tuning in T5 neurons. Knock-down of the nAChRα7 subunit resulted in an increase in calcium responses to both the null and preferred motion direction (Figure 6D). Knock-down of the mAChR-B caused an overall increase of calcium T5 responses across all presented stimuli directions (Figure 6E). Individual fly responses shown in Figure S11D, show that the nAChRα4 and nAChRα5 subunit knock-down flies vary in their responses, whereas the nAChRα7, mAChR-B and mCherry RNAi flies exhibit more stable response patterns. In general, all the AChRs that were tested influence the T5 directional tuning (Figure 6F).

The complexity of cholinergic neurotransmission in T5 cells leads to two distinct niches; the dendritic niche in LO1, where T5-T5 dendro-dendritic synapses[39] reside, and the axonal terminal niche in LOP3, where T4-T5 and T5-T5 axo-axonic synapses reside[87]. Calcium responses in nAChRα5 subunit knock-down flies exhibited different profiles in LO1 and LOP3 (Figure S12A-C). Calcium responses from T5 dendrites were of lower amplitude, while responses from T5 axonal terminals increased in response to the non-preferred (270°) direction in nAChRα5 RNAi compared to control mCherry RNAi flies (Figure S12B,C). Together these experiments show that an interplay of nicotinic and muscarinic receptors shapes the T5 directional responses and suggest a greater complexity among the Tm1-, Tm2-, Tm4-, Tm9-to-T5 connections.

Discussion

In this study, we investigated the acetylcholine receptors that are found in T5 neurons of *Drosophila*. T5 cells express a variety of acetylcholine receptors on their dendrites, which they differentially use across the cholinergic Tm1-, Tm2-, Tm4-, Tm9-to-T5 synapses, marking the first time that postsynaptic differences across the Tm inputs are observed. This acetylcholine receptor variety is translated as a functional variety which is portrayed both in the fly optomotor response and the T5 directional tuning.

Screening of AChR expression in T5 dendrites

In mammals, nicotinic AChRs comprise of nine α (α1-7,9,10), four β (β1-4), one γ, one δ and one ε subunit[88], whilst muscarinic AChRs consist of five M (M1-5) types[89]. This AChR structural variety extends, to a lesser extent, in *Drosophila melanogaster*, with its ten AChR subunits and three mAChR types. For a long time, the expression of AChRs in the visual system of the fruit fly has been under investigation[56,57,90,91,92]. Advancements in genomics and molecular engineering now allow access to the AChRs of interest by endogenously tagging them with fluorescent proteins[22,56,57]. This allows for qualitatively and quantitatively assessing the AChR neuronal expression, and avoiding the ambiguity that was introduced via combinatorial studies of electrophysiology and antagonist application in terms of qualitative AChR identification[93]. With the use of nAChR-tagged fly strains[22], we evaluated the

expression of six out of seven nAChRα subunits on T5 dendrites and identified the nAChRα1, nAChRα4, nAChRα5[56] and nAChRα7 subunit protein localization, which was further supported by RNA sequencing datasets[42,54] and enhancer trap experiments (Figure 1, S1C,D, S4). For the remaining nAChRα3, nAChRβ1, nAChRβ2 and nAChRβ3 subunits, only nAChRα3 and nAChRβ1 should localize in T5 dendrites[54,55,56,58]. Interestingly, the nAChRβ1 subunit has been found to co-localize with the nAChRα1 subunit[56]. Whether this co-localization depicts a pentameric co-organization as previously speculated[92], remains to be proven, but it certainly indicates the stoichiometrical nAChR complexity[94,95] that exists in the optic lobe. For the mAChR-mediated cholinergic neurotransmission, our results together with previous studies[54,55,58] indicate the expression of the mAChR-B type in T5 cells.

Synaptic localization of nAChRα subunits

Sparse neuronal accessibility by light microscopy[64] and electron microscopy reconstructions[59,60,61] enabled us to verify the explicit genetic access to Tm1, Tm2, Tm4 and Tm9 neurons, which allowed for synaptic accessibility via Brp labelling (Figure 2). While mapping the most highly expressed subunits nAChRα1, nAChRα4, nAChRα5 and nAChRα7 across Tm1, Tm2, Tm4 and Tm9 synapses in LO1, we found the nAChRα5 subunit preferentially localizing in Tm1, Tm2, Tm4 rather than Tm9 synapses. This marks the first time that the functional differences that were observed among Tm1, Tm2, Tm4 and Tm9 cells[46,53] are extended to the postsynaptic receptor level. Tm9 is functionally different from Tm1, Tm2 and Tm4 by acting as a low-pass filter[46,47], but it also uses a different nAChR set for its cholinergic neurotransmission. This suggests that the preferred direction enhancement in T5 cells is not only shaped by the different time-courses of the input signals they receive, but it also relies on postsynaptic mechanisms as well. In addition, the mAChR-B localization in Tm9-T5 synapses, together with the nAChRα localization, points towards an interplay between the ionotropic and metabotropic pathways. The role of such receptor interactions is still uncharted, but recent examples indicate that it might potentiate the nicotinic AChR responses[20].

The importance of neuronal input compartmentalization in T5 dendrites has led to combinatorial approaches, where the spatial wiring of inputs together with the receptor dendritic localization was addressed. Together with previous reports[39,49],

our data show a spatial overlap of Tm-to-T5 synapses (Figure 4). It is therefore risky to draw conclusions about receptor localization in T5 dendritic synapses via single-cell receptor localization experiments, especially due to the shared cholinergic nature of the input neurons and their spatial overlap. In this study, we introduce a new methodology, where neuronal input spatial wiring and synaptic receptor mapping are combined to extract pre-, post-synaptic and spatial wiring information. Ultimately, single synapse-to-single dendrite approaches will transform connectivity studies and will help us unravel the T5 AChR-connectome[96].

Effects of AChR knock-downs in the OFF-motion pathway

Do these individual nAChR subunits and mAChR types differentially control the T5 directional computations? When visually activating the OFF-motion pathway, the knock-down of the nAChRα4 and the mAChR-B type resulted in an increase of the fly angular velocity, whereas the nAChRα5 and nAChRα7 knock-down decreased the fly angular velocity under fixed edge velocity conditions. This indicated that both ionotropic and metabotropic pathways are employed for visual processing tasks. Notably, the nAChRα5 and nAChRα7 localization in T5 axonal terminals might result in behavioral alterations deriving from other than simply dendrite-derived computations. As the encountered behavioral output involves many T5 downstream partners[79,97,98], compensatory mechanisms might also be activated, thus potentially masking the T5 immediate effects.

Calcium imaging in T5c neurons revealed an increase in the null direction responses among all nAChRα4, nAChRα5, nAChRα7 and mAChR-B knock-down flies, while only the nAChRα7 and mAChR-B knock-down flies displayed amplified preferred direction responses. We reasoned that the nAChRα5 subunit knock-down, while being the most highly expressed subunit along Tm1, Tm2, Tm4 and Tm9-T5 synapses, would have severely attenuated the T5 preferred direction responses. The T5 dendritic nAChRα5 knock-down effects were milder than expected, probably as an outcome of subunit compensation[99], suggesting an important role for the nAChRα1, nAChRα4 and nAChRα7 subunits in preserving Tm1, Tm2, Tm4 and Tm9-to-T5 function. Lastly, the mAChR-B knock-down-induced effects resemble that of a raised inhibition, which align with the receptor's reported inhibitory role[23]. Our results show that there is an interplay of nicotinic and muscarinic AChRs taking place

on T5 dendrites. The distinct stoichiometries as well as the ionic properties of the nAChR subunits must be identified in the future in order to help us better understand the molecular mechanisms underlying direction selectivity in T5 cells.

Limitations of this study

Multiple aspects should be taken into account when interpreting RNA interference experiments. Firstly, an AChR subunit compensation[99] might take place, concealing the true receptor subunit function. To which extent such a mechanism is activated in T5 neurons, and towards which subunits, is currently unknown. Secondly, the imaging location (T5 dendrites in LO1 versus T5 axonal terminals in LOP) should be considered. T5-T5 dendro-dendritic synapses are cholinergic and so are T5-T5 and T4-T5 axo-axonic synapses[87], relevant for the nAChRα5 and nAChRα7 subunits, hence our interference experiments will affect their function as well, with yet unknown consequences in T5 directional tuning. In an effort to attend this, we observed different responses in T5 dendrites compared to T5 axonal terminals. The difference in dendrite and axon responses could result from differences in the density of ionotropic AChRs and other voltage gated calcium channels between the two T5 compartments or from an uncharacterized influence of T5-T5 dendro-dendritic and T5-T5 and T4-T5 axo-axonic synapses (Figure S12). Finally, even though we used standardized conditions for our RNAi induction experiments, fly-to-fly variability was encountered in nAChRα4 and nAChRα5 knock-down flies (Figure S11). This led us to believe that the RNAi efficiency may differ across individuals and compensation mechanisms at the individual level might be activated.

This study reveals the structural and functional heterogeneity of AChRs in the OFF-motion pathway of *Drosophila.* The nAChRα5 subunit was found to be a key player in the functional distinction of the four columnar T5 cholinergic inputs, while both nicotinic and muscarinic acetylcholine receptors contribute to the OFF-elicited optomotor response and T5 directional tuning.

STAR+METHODS

Detailed methods are provided in the online version of this paper and include the following:

- **KEY RESOURCES TABLE**

- **RESOURCE AVAILABILITY**
  - Lead contact
  - Materials availability
  - Data and code availability

- **EXPERIMENTAL MODEL AND SUBJECT DETAILS**
  - Fly husbandry

- **METHOD DETAILS**
  - Generation of UAS-CRASP line
  - RNAi experiments
  - Immunohistochemistry
  - Confocal microscopy
  - Behavior
  - Two-photon microscopy
  - Visual stimulation
  - Trans-synaptic alignment
  - EM analysis

- **QUANTIFICATION AND STATISTICAL ANALYSIS**
  - nAChRα density
  - Synapse occupancy
  - RNAi efficiency
  - Behavior
  - Calcium imaging
  - Statistical analysis

ACKNOWLEDGMENTS

The authors thank D. Owald, C.H. Lee, F. Pinto-Teixeira, the Bloomington Drosophila Stock Center, the Vienna Drosophila Stock Center and the Developmental Studies Hybridoma Bank for flies and antibodies. We are grateful to the Princeton FlyWire team and members of the Murthy and Seung labs for development and maintenance of FlyWire (supported by BRAIN Initiative grant MH117815 to Murthy and Seung). We are thankful to B. Zuidinga for technical assistance with behavioral experiments and calcium imaging analysis; M. Sauter for technical assistance with fly dissections; S. Prech for technical assistance with experimental setups; R.M. Vieira and J. Pujol-Martí for discussions. E. Samara is a member of the Graduate school of Systemic Neurosciences (GSN) Munich. I.M.A.R. was funded by LMU and the DFG grant nr RI 3644/2-1. This work was funded by the Max Planck Society.

AUTHOR CONTRIBUTIONS

E.S. and A.B. conceived this study. E.S., T.S. and I.M.A.R. designed the experiments. E.S. performed all experiments with the help of T.S. and M.B.L. T.S. contributed to the receptor synaptic localization experiments and analysis. M.B.L contributed to the optomotor response experiments. J.H. contributed to the calcium imaging analysis. E.S. wrote the manuscript with the help of I.M.A.R. and A.B. All authors have read and commented on this manuscript.

DECLARATION OF INTERESTS

The authors declare no competing interests.

FIGURE TITLES AND LEGENDS

Figure 1. AChR expression on T5 dendrites

(A) Schematic representation of T5 dendrites residing in lobula layer 1 (LO1) of the *Drosophila* optic lobe (OL).

(B) Schematic representation of nicotinic ionotropic (magenta) and muscarinic metabotropic AChRs (cyan) in *Drosophila*. Out of the seven nAChRα subunits, six were tagged with EGFP[22]. The mAChR-B was tagged with the HA peptide tag (C.H.Lee)

(C) OL (grey) with T4 and T5 dendrites (R42F06-Gal4>UAS-myr::tdTomato, blue) in M10 and LO1 accordingly. Scale bar 40µm.

(D-l) nAChRα1, nAChRα2, nAChRα4, nAChRα5, nAChRα6 and nAChRα7 (nAChRα::EGFP, magenta) subunit expression on T5 dendrites (R42F06-Gal4>UAS-myr::tdTomato, blue). Scale bar 10µm, inset 5µm.

(J) Density of nAChRα subunit expression on T5 dendrites across 30 ROIs in LO1 (optic lobes n=6). nAChRα3, nAChRβ1, nAChRβ2 and nAChRβ3 subunits were not addressed. Subunits with the lowest expression levels are in grey. Data is mean ± SEM.

(K) Overexpression of mAChR-B (UAS-mAChR-B::HA, cyan) on T5 dendrites (R42F06-Gal4>UAS-myr::tdTomato, blue). Scale bar 10µm, inset 5µm.

Figure 2. Morphological identification of the four columnar T5 cholinergic input neurons

(A) Electron microscopy (EM)(flywire.ai) reconstruction of a Tm1 neuron reveals two loci of arborization in medulla. Schematic representation of the Tm1 axonal terminal localization in LO1. Tm1-Gal4 expression (cyan) of the MultiColor FlpOut cassette (V5, HA, FLAG) and axonal localization in LO. Scale bar 40µm and 10µm.

(B) Whole population labelling of Tm1 neurons (R74G01-Gal4>UAS-CD8::GFP). Scale bar 40µm.

(C) Whole population labelling of Tm1-LexA (purple) neurons (VT041034-LexAGAD>LexAop-myr::mCherry). Arrows represent additional dendritic ramifications that lack in (B). Scale bar 40µm.

(D-F) As in (A-C), but for Tm2 neurons (VT012282-Gal4, VT058650-LexAGAD).

(G-I) As in (A-C), but for Tm4 neurons (R35H01-Gal4, R53C02-LexAGAD).

(J-L) As in (A-C), but for Tm9 neurons (VT065303-Gal4, R24C08-LexAp65).

Figure 3. Differential synaptic localization of nAChRα subunits in Tm synapses

(A-D) Trans-synaptic alignment of Tm1, Tm2, Tm4 and Tm9 boutons (Tm-Gal4> UAS-Brp$^{short::mStraw}$, grey) with the nAChRα1, nAChRα4, nAChRα5 and nAChRα7 subunits (nAChRα::EGFP, magenta) in LO1. Arrows indicate the Brp$^{short::mStraw}$-receptor punctum trans-synaptic alignment. Scale bar 1µm.

(E-H) Synapse occupancy of Tm1, Tm2, Tm4 and Tm9 boutons with nAChRα1 (pale magenta), nAChRα4 (light magenta), nAChRα5 (magenta) and nAChRα7 (dark magenta) subunits in LO1 (optic lobes n=4, ROIs N=20, for Tm4-nAChRα5 n=3, N=15). Data is mean ± SEM.

Figure 4. Wiring of Tm1, Tm2, Tm4 and Tm9 on T5 dendrites

(A) Counts of Tm1, Tm2, Tm4 and Tm9 synapses in T5a dendrites (T5a cells n=5, flywire.ai) (left). Counts of predicted (n=663) to proofread (n=479) Tm synapses in T5a dendrites (right). Data is mean ± SEM.

(B) As in (A) for T5c dendrites (T5c cells n=5, flywire.ai) (left). Counts of predicted (n=621) to proofread (n=488) Tm synapses in T5c dendrites (right). Data is mean ± SEM.

(C) Dendritic localization of Tm synapses across the T5a anterior-posterior axis (T5a cells n=5). Root is considered the first dendritic branch point.

(D) Dendritic localization of Tm synapses across the T5c dorso-ventral axis (T5c cells n=5).

(E) Schematic representation of Tm-T5a dendritic synapses and the observed postsynaptic receptor heterogeneity in terms of the most abundant nAChR subunit as in Figure 3E-H.

Figure 5. Fly optomotor response post-AChR knock-down

(A) Schematic workflow representation for the behavioral assessment of AChR knock-down flies.

(B) Trajectory (angular velocity) of nAChRα1 knock-down flies (R42F06-p65.AD; VT043070-Gal4.DBD>UAS-nAChRα1-RNAi, pale magenta, flies n=20) while presented to a sequence of upward to rightward to downward to leftward OFF edge motion compared to the parental control flies (UAS-nAChRα1-RNAi, grey n=21). The dark lines represent the mean ± SEM.

(C-F) Same as in (B) for the nAChRα4 (light magenta n=19, grey n=20), nAChRα5 (magenta n=18, grey n=21), nAChRα7 (dark magenta, n=21, grey n=20), mAChR-B (cyan n=20, grey n=20) knock-down flies.

(G) Angular velocity of control and AChR knock-down flies. The normality of distribution was assessed with the use of Shapiro-Wilk test. *$p<0.05$, **$p<0.01$, ***$p<0.001$. Data is mean ± SEM.

Figure 6. Directional tuning of T5 cells post-AChR knock-down

(A) Schematic workflow representation for the two-photon calcium imaging in AChR knock-down T5 cells.

(B) Polar plot of the maximum responses (ΔF/F) across sixteen OFF edge directions (º) of T5c cells for mCherry controls (black, flies n=7, ROIs N=85, shown as grey in C, D and E) and nAChRα4 RNAi (light magenta, n=7, N=61) conditions (R39H12-Gal4>AChR-RNAi, VT50384-LexA>LexAop-IVS-GCaMP6m). The dark lines represent the mean (68% CI).

(C) Same as in (B) for nAChRα5 RNAi flies (magenta, n=7, N=82).

(D) Same as in (B) for nAChRα7 RNAi flies (dark magenta, n=7, N=60).

(E) Same as in (B) for mAChR-B RNAi flies (cyan, n=7, N=54).

(F) Directional tuning index. N_{ROIs} as in B-E. The normality of distribution was assessed with the use of Shapiro-Wilk test. ***p<0.001, ****p<0.0001. Data is mean ± SEM.

STAR Methods

RESOURCE AVAILABILITY

Lead contact

Further information and requests for data should be directed to and will be fulfilled by the Lead Contact, Alexander Borst (alexander.borst@bi.mpg.de).

Materials availability

The study generated a new fly line and is available from lead contact upon request.

Data and code availability

- This paper analyzes existing, publicly available data from FlyWire (flywire.ai).
- Data and code for analysis are publicly available at the at the Edmond Open Research Data Repository of the Max Planck Society.
- Any additional information required to reanalyze the data reported in this paper is available from the lead contact upon request.

EXPERIMENTAL MODEL AND SUBJECT DETAILS

Fly husbandry

All flies were raised on corneal agar medium under standard conditions (25°C, 60% humidity, 12h light/dark cycle). For the interference experiments (RNAi), flies (control and RNAi) at early pupa stages were transferred from 25 to 29°C. For the Multi-color FlpOut experiments, flies at early pupa stages were heat-shocked for 30 minutes at 37°C.

METHOD DETAILS

Generation of UAS-CRASP line

The pQUAST-syb-spCFP1-10 vector[72] and the pJFRC7-20XUAS-IVS-mCD8::GFP vector[100] were digested with XhoI and XbaI restriction enzymes and the syb-spCFP1-10 DNA fragment was extracted and T4-ligated in the pJFRC7 vector. The AGGCACACCGAAACGACTAA and CAGTTCCATAGGTTGGAATCTAAAA primers were used for sequencing the successful insertion of the DNA fragment. Embryo injections were performed by BestGene Inc (Chino Hills, CA, USA) in the VK00027 attp landing site.

RNAi experiments

To ensure high interference efficiency, given that both long dsRNA (nAChRα1, nAChRα4 and nAChRβ1) and short shRNA (nAChRα3, nAChRα5 and nAChRα7, mAChR-A, mAChR-B) were used, flies were raised (at early pupa stages) at 29°C[84,85] and the RNAi was induced prior to the receptor expression peak. Dicer was not used for the long dsRNA experiments as previous studies[22,101,102] showed positive AChR-RNAi induction without dicer co-expression. Our immunohistochemical screening spoke in favor of the nAChRα1, nAChRα4, nAChRα5, nAChRα7 and mAChR-B RNAi effectiveness (Figure S3).

Immunohistochemistry

Fly brains (aged 2-5 days, for G-and C-RASP experiments aged 10-12 days) were dissected in cold phosphate-buffered saline (PBS) and fixed in 4% paraformaldehyde (in PBS with 0.1% Triton X-100) for 24 minutes at room temperature, followed by three 10-minute washes in PBT (PBS and 0.3% Triton X-100). Brains were then incubated with primary antibodies in PBT for 48 hours at 4°C. After being incubated for 2 hours at room temperature, brains were washed four times for 15 minutes each in PBT and then incubated with secondary antibodies diluted in PBT for 48 hours at 4°C. After being incubated for 2 hours at room temperature and four 15 minutes PBT washes, brains were mounted for immediate sample viewing. For the subunit mapping (Figure 3), brains were blocked in 5% normal goat serum (NGS) in PBT for 1 hour at room temperature and then incubated with the primary and secondary antibodies for 24 hours instead of 48 hours.

Confocal microscopy

Images were acquired in a Leica Stellaris 5 laser scanning confocal microscope with a 20x glycerol 0.75 NA HC Plan-apochromat and 63x glycerol immersive 1.3 NA HC Plan-apochromat objective at 2048 x 2048 x 0.4μm image resolution. The deconvolution setting (Lightning) of this microscope was used for the acquisitions in Figure 3. Image analysis was performed with Fiji (ImageJ)[103]. For the acquisitions in Figure S4, a Leica SP8 laser scanning confocal microscope with a 63x oil immersive 1.3 NA HCX Plan-apochromat objective was used at 2048 x 2048 x 0.4μm image resolution.

Behavior

To avoid behavioral effects introduced by sexual dimorphism[26], only female flies, 1-3 days old, were used in our experiments. Flies were attached to a pin post-cold anaesthetization with the use of light-curing glue and dental curing light (440 nm, New Woodpecker). Each locomotor recorder, out of the four that were simultaneously used, consisted of an air-suspended sphere (6mm in diameter and 40 mg weight) made of polyurethane foam and coated with polyurethane spray[81,104]. A constant airflow by a rotary vane pump (G6/01-K-EB9L Gardner Denver Thomas) allowed for the free rotation of the sphere on the ball-shaped sphere holder. The sphere's rotation was tracked by two optical tracking sensors, focusing two 1-mm^2 equatorial spots at ±30° from the center of the infrared LED-illuminated (JET-800-10, Roithner Electronics) sphere. Rotational data were tracked at 4 kHz and digitized at 200 Hz[105]. To achieve a successful fly positioning on the sphere, a camera (GRAS-20S4M-C, Point Grey Research) was used. A custom-made Peltier system (QC-127-1.4-6.0MS, Quick-Cool) controlled the airflow temperature at 34 ± 0.1°C, based on the readouts deriving from a thermometer placed just below the sphere, so as to ensure prolonged walking. A U-shaped visual arena comprising of three 120-Hz LCD screens (Samsung 2233 RZ) (reaching a maximum luminance of 131 cd m^{-2}), allowed for the presentation of visual stimuli spanning approximately 270° in azimuth and 120° in elevation of the fly's visual field at a resolution of <0.1°. Panda3D was used in Python v.2.7 for the visual stimulus generation[81].

Two-photon microscopy

For functional imaging experiments, we used a custom-build two photon laser scanning microscope equipped with a 40x water 0.80 NA IR-Achroplan objective

(Zeiss)[33]. Flies (1-3 days) were cold-anaesthetized and the legs and thorax were glued on a Plexiglas holder with the use of light-curing glue. The head was bend down, fitted in an aluminum opening and the holder was clamped in a recording chamber. Saline solution (PBS; 137 mM NaCl, 3 mM KCl, 8 mM Na_2HPO_4, 1.5 mM KH_2PO_4, pH 7.3) was introduced and the posterior side of the fly's optic lobe was exposed by a small incision of the head. Muscles, adipose tissue and trachea were manually removed. Images were acquired at a 64 x 64-pixel resolution and a frame rate of 15 Hz in Matlab R2013b (MathWorks) using ScanImage 3.8 software (Vidrio Technologies, LLC).

Visual stimulation

For the behavioral experiments, OFF edges (50% contrast) moved at 16 evenly spaced directions with a velocity of 60° s^{-1}, were randomized and crossed the whole arena span within 5s. Each experiment lasted for ~55 min, including 35 trials of OFF edges, of which the first 15 trials were excluded from analysis, as they were appointed to temperature stabilization and fly accommodation. The same inclusion criteria as in a previous study[44] were used.

For the calcium imaging experiments, we used a custom-built projector-based arena[53], where two micro-projectors (TI DLP Lightcrafter 3000) projected visual stimuli, with a refresh rate of 180 Hz and maximum luminance of 276 ± 48 cd/m^2, onto the back of a cylindrical screen. The arena covered 180° in azimuth and 105° in elevation of the fly's visual field. OFF edges (92% contrast) moved at 16 evenly spaced directions with a velocity of 30° s^{-1}, were randomized and repeated four times.

Trans-synaptic alignment

To assess the trans-synaptic alignment between the receptors and the synapses of interest, we calculated the fluorescence intensity values (later normalized to the maximum pixel intensity value) in a 1 µm line positioned across the synapse punctum in a single z plane using Fiji-ImageJ[103]. Data analysis was performed with Python v.3.9.18 with the use of seaborn 0.12.2, pandas 1.5.3 and numpy 1.23.3.

EM analysis

For the Tm-T5 wiring, we used the FAFB volume[59] via the FlyWire (flywire.ai) proofreading environment[60,61] and chose five reconstructed T5a and five T5c neurons from the right optic lobe (Table S3). T5 and Tm1, Tm2, Tm4, Tm9 identities were verified by users' annotations and by comparison with previous electron microscopy[39] and our light microscopy reconstructions. Synapse number Buhmann predictions[75,76] between the T5 neuron of interest and its respective input neurons were acquired from FlyWire's connectivity viewer. Cleft score was set to 50, so as to eliminate synaptic redundancy resulting from the combination of synaptic connections between the same neurons when their presynaptic locations are within $100nm^2$. For each synapse, we sought four morphological markers: a. synaptic vesicles, b. the protein dense T-bar structure, c. synaptic cleft, and d. postsynaptic densities (or postsynaptic domains). Every synaptic locus was assessed in a volume of five up to seven brain slices, 40nm each. Only synapses that displayed all four morphological markers were included in our dataset. We treated proofread synapses as points in T5 dendrite space by collecting the x,y,z coordinates of each T-bar (pre-synapse). Synapse numbers in this study correspond to manually proofread synapses.

For synapse distributions across the anterior-posterior and dorso-ventral dendritic arborization axis (Figure 4C,D), we measured the Euclidean distance of every synapse from the root (first branching point) of the dendrite. Distances in µm were calculated by multiplying the y and z coordinates of each T-bar with 4 and 40 accordingly (voxel=4x4x40nm). To correct for anterior-posterior and dorsal-ventral dendrite length differences, we normalized each synapse-to-root Euclidean distance to the longest T5a and T5c dendrite.

For the identification of Tm1, Tm2, Tm4 and Tm9 synaptic partners in LO1 (Figure S8), we used Codex[59,60,61]. We searched for all the Tm output neurons in five Tm1 (FlyWire ID: 720575940620976493,720575940608883465,720575940623583428, 720575940632600647,720575940621146733), Tm2 (FlyWire ID: 720575940632142904,720575940640453437,720575940640230259,720575940630551670,720575940622364961), Tm4 (FlyWire ID: 720575940637976666, 720575940620745163, 720575940621582401, 720575940626612228, 720575940620782171) and Tm9 (FlyWire ID: 720575940613374873, 720575940620814356, 720575940609254851,

720575940626242348, 720575940623771061) cells, and selected only those outputs whose Tm synapses were restricted in LO1 (excluding all Tm medullary output neurons). For the output neurons that only formed connections with Tm neurons in LO1, we used the predicted synapse number, but for those output neurons that made Tm connections in other LO layers as well, we manually proofread the LO1 synapses. The reconstructed neurons for Figure 2 correspond to FlyWire IDs 720575940621338038, 720575940614527742, 720575940616041926 and 720575940616813142 for Tm1, Tm2, Tm4 and Tm9 respectively.

QUANTIFICATION AND STATISTICAL ANALYSIS

nAChRα density

Receptor puncta that localized in T5 dendrites were quantified along 8µm x 8µm x 4µm voxels in Fiji-ImageJ[103]. The total number of puncta divided to the analyzed LO1 volume resulted in the nAChRα density.

Synapse occupancy

The total number of Brp-receptor co-localizing puncta in voxels of 8µm x 8µm x 4µm in Fiji-ImageJ[103], was divided to the number of Brp puncta, resulting in the synapse occupancy index.

RNAi efficiency

The mean grey value of ten 8µm x 8µm ROIs per optic lobe in LO1 and LOP (layer 1 and 2) was measured via Fiji-ImageJ[103] and was normalized by subtracting the mean grey value of one 8µm x 8µm ROI in the inner optic chiasm.

Behavior

The optomotor response was quantified as the absolute average rotational velocity during 5 s of edge motion in each direction. Data analysis was performed with Python v.3.9.18 using seaborn 0.12.2, pandas 1.5.3 and numpy 1.23.3.

Calcium imaging

Calcium imaging data were analyzed as described in[53] with a custom written software in Python v.2.7. ROIs were drawn manually across LO layer 1 and LOP

layer 3. Only ROIs that repeatedly responded to the given visual stimulus and exhibited consistent-across the four repetitions-responses, were included in the dataset. For each ROI, the time courses of relative fluorescence changes (ΔF/F) were calculated and responses to stimulus were baseline-subtracted and averaged over repetitions. Maximum responses were aligned to 90°. The directional tuning index (Figure 6F, Ldir) was calculated as the magnitude of the resultant vector divided by the sum of the individual vectors' magnitudes:

$$Ldir = \left| \frac{\sum_{\varphi} \overrightarrow{v(\varphi)}}{\sum_{\varphi} \overrightarrow{|v(\varphi)|}} \right|$$

Statistical analysis

Detailed analysis is reported in figure legends and table S2 and was performed in GraphPad Prism v.9.3.0.

SUPPLEMENTAL INFORMATION TITLES AND LEGENDS

Figure S1. AChR expression in T5 cells-Related to Figure 1

(A) nAChRα2 expression in LO. Arrows indicate the LO layers of expression. Scale bar 10μm, inset 5μm.

(B) Example ROIs in LO1 for quantification as in Figure 1J. Scale bar 10μm, inset 5μm.

(C) Bulk RNAseq of AChR expression (transcripts per million, TPM) in T5 cells and probability of expression (p)[42].

(D) scRNAseq of AChR expression in T4 (grey) and T5 (blue) cells across five developmental stages (hours correspond to APF-after puparium formation)[54].

Figure S2. AChR expression in T4-T5 axonal terminals-Related to Figure 1

(A) Schematic representation of T5 axonal terminals residing in lobula plate (LOP1-4) of the *Drosophila* optic lobe (OL).

(B-G) Expression of nAChRα1, nAChRα2, nAChRα4, nAChRα5, nAChRα6 and nAChRα7 (nAChRα::EGFP, magenta) in T4-T5 axonal terminals (R42F06-Gal4>UAS-myr::tdTomato, blue). Scale bar 10μm.

(H) Overexpression of mAChR-B (cyan) in T4-T5 axonal terminals (R42F06-Gal4>UAS-myr::tdTomato, UAS-mAChR-B::HA). Scale bar 10μm.

(I) Pan-neuronal expression of mAChR-B in OL (GMR57C10-Gal4>UAS-mAChR-B::HA). Scale bar 40µm.

(J) Normalized mean grey value of nAChR subunits in LOP (layers 1 and 2) before and after RNAi induction (optic lobes n=2, ROIs N=20, for nAChRα1 n=1). The normality of distribution was assessed with the use of Shapiro-Wilk test. *p<0.05, ****p<0.0001. Data is mean ± SEM.

(K) Summarized expression patterns of nAChRα1, nAChRα2, nAChRα4, nAChRα5, nAChRα6 and nAChRα7 subunits and the mAChR-B type on T5 dendrites and in T4-T5 axonal terminals.

Figure S3. RNA interference against AChRs in T5 cells-Related to Figure 1 and 5

(A) Expression of the nAChRα1 subunit (nAChRα1::EGFP) in LO1 before (left panel) and after (right panel) the RNAi induction (R42F06-Gal4>AChR-RNAi). Scale bar 10µm.

(B-E) As in (A) for the nAChRα4, nAChRα5, nAChRα7 subunits and the mAChR-B type.

(F) Normalized mean grey value of AChRs in LO1 before and after RNAi induction (optic lobes n=2, ROIs N=20). The normality of distribution was assessed with the use of Shapiro-Wilk test. **p<0.01, ***p<0.001, ****p<0.0001. Data is mean ± SEM.

(G) Developmental onset (P18) of the R42F06 promoter used for the split T4-T5 line in all behavioral experiments (R42F06-Gal4> UAS-myr::tdTomato). Scale bar 40µm, inset 10µm.

(H) Split T4-T5 line (R42F06-p65.AD; VT043070-Gal4.DBD>UAS-CD4::tdGFP) used in all behavioral experiments. Arrows indicate the four LOP layers. Scale bar 40µm, inset 10µm.

Figure S4. Enhancer-trap verification of AChR expression in T4-T5 cells-Related to Figure 1

(A-L) Enhancer-trap lines for the nAChRα1, nAChRα2, nAChRα3, nAChRα4, nAChRα5, nAChRα6, nAChRα7, nAChRβ1, nAChRβ2, nAChRβ3 subunits and mAChR-A and mAChR-B receptors (AChR-Mi or T2A-Gal4>UAS-CD8::GFP, magenta and cyan). Signal overlap with T4-T5 somata (R42F06-LexA>LexAop-CD8::RFP, blue) denoted the T4-T5 AChR expression. The nAChRα4 line did not show expression across all brain areas. Images are z-projections. Scale bar 40µm, inset 10µm.

(M) AChR expression in T5 cells across scRNA-seq[54], Bulk-seq[42], enhancer trap and endogenously tagged receptor[56] experiments.

Figure S5. Screening of genetic approaches for synapse visualization-Related to Figure 3

(A) Membrane-targeted GFP expression in Tm1, Tm2, Tm4 and Tm9 axonal terminals (Tm1, Tm2, Tm4, Tm9-Gal4>UAS-CD4::tdGFP). Scale bar 10µm.

(B) Brp^{short}::GFP expression in Tm1, Tm2, Tm4 and Tm9 boutons (Tm1, Tm2, Tm4, Tm9-Gal4>UAS-Brp^{short}::GFP). Scale bar 10µm.

(C) t-GRASP expression in Tm1, Tm2, Tm4 and Tm9-T5 synapses (Tm1, Tm2, Tm4, Tm9-Gal4>UAS-pre-t-GRASP, VT25965-LexAp65>LexAop-post-t-GRASP). Scale bar 10µm. Ectopic reconstitution is observed in Tm4-T5 synapses.

(D) Activity GRASP (syb-GRASP) in Tm1, Tm2, Tm4 and Tm9-T5 synapses (Tm1, Tm2, Tm4, Tm9-Gal4>UAS-nSyb-spGFP1-10, VT25965-LexAp65>LexAop-CD4-spGFP11). Scale bar 10µm.

Figure S6. Validation of Brp^{short} as a precise presynaptic marker-Related to Figure 3

(A) Trans-synaptic alignment between $Brp^{short::mCherry}$(blue) and the GABAergic Rdl receptor (grey) in the cholinergic Tm3-T4 synapse (GMR13E12-LexA>LexAop-Brp^{short}::mCherry, R42F06-Gal4>UAS-Rdl::GFP). Scale bar 10µm.

(B) Trans-synaptic alignment between $Brp^{short::mCherry}$(blue) and the glutamatergic GluClα receptor (grey) in the glutamatergic Mi9-T4 synapse (GMR48A07-LexA>LexAop-Brp^{short}::mCherry, R42F06-Gal4>UAS-GluClα::GFP). Scale bar 10µm.

(C) Localization of $Brp^{short::mStraw}$ in Tm1, Tm2, Tm4 and Tm9 boutons (blue) and endogenous Brp (grey) identified by the anti-Brp staining. Arrows correspond to the signal overlap between the Tm-Brp^{short} and the Anti-Brp. Scale bar 5 and 1µm.

Figure S7. Localization of nAChRα subunits in Tm synapses-Related to Figure 3

(A) LO1 loci that were used for Figure 3A-D. Scale bar 10µm.

(B) Line profile analysis for the assessment of trans-synaptic alignment of $Brp^{short::mStraw}$ puncta (grey) and nAChRα puncta (magenta) across Tm1, Tm2, Tm4 and Tm9 synapses (analyzed puncta n=10). The dark lines represent the mean values.

Figure S8. Neuronal outputs of Tm1, Tm2, Tm4 and Tm9 cells in LO1-Related to Figure 3

(A) Schematic representation of Tm1, Tm2, Tm4 and Tm9 axonal terminals in relation to LO1. Primary Tm1, Tm2, Tm4 and Tm9 output neuronal types in LO1 (Tm cells n=5, Codex). Data is mean ± SEM.

(B) C-RASP for the Tm9-T5 synapse visualization (Tm9-Gal4>UAS-IVS-syb-spCFP1-10, VT25965-LexAp65>LexAop-CD4-spGFP11, grey) of the nAChRα7 subunit (nAChRα7::EGFP, magenta). Arrows correspond to Tm9-nAChRα7 trans-synaptic alignment. Scale bar 10μm.

Figure S9. mAChR-B receptor localization in T5 dendrites-Related to Figure 3

(A) mAChR-B localization (R42F06-Gal4>UAS-mAChR-B::HA, cyan) in Tm9-T5 synapses (Tm9-LexA>LexAop-Brp^{short}::mCherry, grey). Scale bar 10μm.

(B) nAChRα5 subunit (nAChRα5::EGFP, magenta) localization pattern compared to mAChR-B (R42F06-Gal4>UAS-mAChR-B::HA, cyan) in LO1. Scale bar 10μm.

Figure S10. Fly optomotor response after nAChRα3, nAChRβ1 and mAChR-A knock-down-Related to Figure 5

(A) Schematic representation of the behavioral setup for the optomotor response assessment in nAChRα3 (pale magenta), nAChRβ1 (violet) subunits and mAChR-A (teal) type knock-down flies.

(B) Trajectory (angular velocity) of nAChRα3 knock-down flies (42F06-p65.AD; VT043070-Gal4.DBD>UAS-nAChRα3-RNAi, pale magenta n=18) while presented to a sequence of upward to rightward to downward to leftward OFF edge motion compared to the parental control flies (UAS-nAChRα3-RNAi, grey n=20). The dark lines represent the mean ± SEM.

(C-D) Same as previously for the nAChRβ1 (violet n=18, grey n=19) and mAChR-A (teal n=20, grey n=20) knock-down flies.

(E) Angular velocity of control and AChR knock-down flies. The normality of distribution was assessed with the use of Shapiro-Wilk test. Data is mean ± SEM.

Figure S11. Two-photon calcium imaging in T5 cells-Related to Figure 6

(A) Schematic representation of LO1 (where T5 dendrites reside) and of LOP3 (where T5c axonal terminals reside).

(B) Two-photon view of LOP3 (VT50384-LexA>LexAop-IVS-GCaMP6m).

(C) T4-T5c specific targeting (VT50384-Gal4>UAS-CD8::GFP). Arrows indicate the four LOP layers. Scale bars 40 and 10μm.

(D) Polar plots of the maximum responses (ΔF/F) -along seven flies- across sixteen OFF edge directions (^{o}) of T5c cells under nAChRα4 RNAi (light magenta), nAChRα5 RNAi (magenta), nAChRα7 RNAi (dark magenta), mAChR-B RNAi (cyan) and control mCherry RNAi (black) conditions.

Figure S12. Two-photon calcium imaging in T5 dendrites and T5 axonal terminals-Related to Figure 6

(A) Schematic representation of LO1 (where T5 dendrites reside) and of LOP3 (where T5c axonal terminals reside).

(B) Two-photon view of the LO1 and LOP3 layers (VT50384-LexA>LexAop-IVS-GCaMP6m).

(C) Polar plots of the maximum responses (ΔF/F) across sixteen OFF edge directions (^{o}) of T5c cells under mCherry controls (black, flies n=5, ROIs N=10) and nAChRα5 RNAi (magenta, n=5, N=13) conditions in LO1 (left) and in LOP3 (right). The dark lines represent the mean (68% CI).

Table S1. List of fly experimental genotypes, related to STAR Methods.

Table S2. Statistical analysis, related to STAR Methods.

Table S3. FlyWire neuronal IDs, related to STAR Methods.

REFERENCES

1. Shin, M., Copeland, J.M., and Venton, B.J. (2018). *Drosophila* as a model system for neurotransmitter measurements. ACS Chem. Neurosci. *9*, 1872–1883. https://doi.org/10.1021/acschemneuro.7b00456.

2. Stuart, A.E. (1999). From fruit flies to barnacles, histamine is the neurotransmitter of arthropod photoreceptors. Neuron *22*, 431–433. https://doi.org/10.1016/S0896-6273(00)80699-6.

3. Kolodziejczyk, A., Sun, X., Meinertzhagen, I.A., and Nässel, D.R. (2008). Glutamate, GABA and acetylcholine signalling components in the lamina of the *Drosophila* visual system. PLoS ONE *3*, e2110. https://doi.org/10.1371/journal.pone.0002110.

4. Yasuyama, K., and Salvaterra, P.M. (1999). Localization of choline acetyltransferase-expressing neurons in *Drosophila* nervous system. Microsc. Res. Tech. *45*, 65–79. https://doi.org/10.1002/(SICI)1097-0029(19990415)45:2<65::AID-JEMT2>3.0.CO;2-0.

5. Eckstein, N., Bates, A.S., Champion, A., Du, M., Yin, Y., Schlegel, P., Lu, A.K.-Y., Rymer, T., Finley-May, S., Paterson, T., et al. (2024). Neurotransmitter classification from electron microscopy images at synaptic sites in *Drosophila melanogaster*. Cell *187*, 2574-2594.e23. https://doi.org/10.1016/j.cell.2024.03.016.

6. Breer, H., and Sattelle, D.B. (1987). Molecular properties and functions of insect acetylcholine receptors. J. Insect Physiol. *33*, 771–790. https://doi.org/10.1016/0022-1910(87)90025-4.

1023 7. Sattelle, D.B., Jones, A.K., Sattelle, B.M., Matsuda, K., Reenan, R., and Biggin, P.C. (2005).
1024 Edit, cut and paste in the nicotinic acetylcholine receptor gene family of *Drosophila*
1025 *melanogaster*. BioEssays *27*, 366–376. https://doi.org/10.1002/bies.20207.

1026 8. Rosenthal, J.S., and Yuan, Q. (2021). Constructing and tuning excitatory cholinergic
1027 synapses: The multifaceted functions of nicotinic acetylcholine receptors in *Drosophila*
1028 Neural Development and Physiology. Front. Cell. Neurosci. *15*, 720560.
1029 https://doi.org/10.3389/fncel.2021.720560.

1030 9. Thany, S.H., Lenaers, G., Raymond-Delpech, V., Sattelle, D.B., and Lapied, B. (2007).
1031 Exploring the pharmacological properties of insect nicotinic acetylcholine receptors.
1032 Trends Pharmacol. Sci. *28*, 14–22. https://doi.org/10.1016/j.tips.2006.11.006.

1033 10. Faltine-Gonzalez, D.Z., and Layden, M.J. (2018). The origin and evolution of acetylcholine
1034 signalling through AchRs in metazoans. Preprint, https://doi.org/10.1101/424804
1035 https://doi.org/10.1101/424804.

1036 11. Littleton, J.T., and Ganetzky, B. (2000). Ion channels and synaptic organization: analysis
1037 of the *Drosophila* genome. Neuron *26*, 35–43. https://doi.org/10.1016/s0896-
1038 6273(00)81135-6.

1039 12. Thompson, A.J., Lester, H.A., and Lummis, S.C.R. (2010). The structural basis of function
1040 in Cys-loop receptors. Q. Rev. Biophys. *43*, 449–499. https://doi.org/10.1017/
1041 S0033583510000168.

1042 13. Dupuis, J., Louis, T., Gauthier, M., and Raymond, V. (2012). Insights from honeybee (*Apis*
1043 *mellifera*) and fly (*Drosophila melanogaster*) nicotinic acetylcholine receptors: From
1044 genes to behavioral functions. Neurosci. Biobehav. Rev. *36*, 1553–1564. https://doi.org/
1045 10.1016/j.neubiorev.2012.04.003.

1046 14. Bielopolski, N., Amin, H., Apostolopoulou, A.A., Rozenfeld, E., Lerner, H., Huetteroth, W.,
1047 Lin, A.C., and Parnas, M. (2019). Inhibitory muscarinic acetylcholine receptors enhance
1048 aversive olfactory learning in adult *Drosophila*. eLife *8*, e48264. https://doi.org/
1049 10.7554/eLife.48264.

1050 15. Malloy, C.A., Somasundaram, E., Omar, A., Bhutto, U., Medley, M., Dzubuk, N., and
1051 Cooper, R.L. (2019). Pharmacological identification of cholinergic receptor subtypes:
1052 modulation of locomotion and neural circuit excitability in *Drosophila* larvae.
1053 Neuroscience *411*, 47–64. https://doi.org/10.1016/j.neuroscience.2019.05.016.

1054 16. Xia, R. -Y., Li, M. -Q., Wu, Y. -S., Qi, Y. -X., Ye, G. -Y., and Huang, J. (2016). A new family of
1055 insect muscarinic acetylcholine receptors. Insect Mol. Biol. *25*, 362–369. https://doi.org/
1056 10.1111/imb.12229.

1057 17. Collin, C., Hauser, F., De Valdivia, E.G., Li, S., Reisenberger, J., Carlsen, E.M.M., Khan, Z.,
1058 Hansen, N.Ø., Puhm, F., Søndergaard, L., et al. (2013). Two types of muscarinic
1059 acetylcholine receptors in *Drosophila* and other arthropods. Cell. Mol. Life Sci. *70*, 3231–
1060 3242. https://doi.org/10.1007/s00018-013-1334-0.

1061 18. Ren, G.R., Folke, J., Hauser, F., Li, S., and Grimmelikhuijzen, C.J.P. (2015). The A- and B-
1062 type muscarinic acetylcholine receptors from *Drosophila melanogaster* couple to
1063 different second messenger pathways. Biochem. Biophys. Res. Commun. *462*, 358–364.
1064 https://doi.org/10.1016/j.bbrc.2015.04.141.

1065 19. Perry, T., Chen, W., Ghazali, R., Yang, Y.T., Christesen, D., Martelli, F., Lumb, C., Bao
1066 Luong, H.N., Mitchell, J., Holien, J.K., et al. (2021). Role of nicotinic acetylcholine
1067 receptor subunits in the mode of action of neonicotinoid, sulfoximine and spinosyn
1068 insecticides in *Drosophila melanogaster*. Insect Biochem. Mol. Biol. *131*, 103547.
1069 https://doi.org/ 10.1016/j.ibmb.2021.103547.

1070 20. Rozenfeld, E., Tauber, M., Ben-Chaim, Y., and Parnas, M. (2021). GPCR voltage
1071 dependence controls neuronal plasticity and behavior. Nat. Commun. *12*, 7252.
1072 https://doi.org/10.1038/s41467-021-27593-x.

1073 21. Manoim, J.E., Davidson, A.M., Weiss, S., Hige, T., and Parnas, M. (2022). Lateral axonal
1074 modulation is required for stimulus-specific olfactory conditioning in *Drosophila*. Curr.
1075 Biol. CB *32*, 4438-4450.e5. https://doi.org/10.1016/j.cub.2022.09.007.

1076 22. Pribbenow, C., Chen, Y., Heim, M.-M., Laber, D., Reubold, S., Reynolds, E., Balles, I.,
1077 Fernández-d V Alquicira, T., Suárez-Grimalt, R., Scheunemann, L., et al. (2022).
1078 Postsynaptic plasticity of cholinergic synapses underlies the induction and expression of
1079 appetitive and familiarity memories in *Drosophila*. eLife *11*, e80445. https://doi.org/
1080 10.7554/eLife.80445.

1081 23. Qin, B., Humberg, T.-H., Kim, A., Kim, H.S., Short, J., Diao, F., White, B.H., Sprecher, S.G.,
1082 and Yuan, Q. (2019). Muscarinic acetylcholine receptor signaling generates OFF
1083 selectivity in a simple visual circuit. Nat. Commun. *10*, 4093.
1084 https://doi.org/10.1038/s41467-019-12104-w.

1085 24. Schlegel, P., Yin, Y., Bates, A.S., Dorkenwald, S., Eichler, K., Brooks, P., Han, D.S., Gkantia,
1086 M., Dos Santos, M., Munnelly, E.J., et al. (2023). Whole-brain annotation and multi-
1087 connectome cell typing quantifies circuit stereotypy in *Drosophila*. Preprint,
1088 https://doi.org/10.1101/2023.06.27.546055.

1089 25. Borst, A., and Euler, T. (2011). Seeing things in motion: Models, circuits, and
1090 mechanisms. Neuron *71*, 974–994. https://doi.org/10.1016/j.neuron.2011.08.031.

1091 26. Surkova, S., Görne, J., Nuzhdin, S., and Samsonova, M. (2021). Interplay between sex
1092 determination cascade and major signaling pathways during *Drosophila* eye
1093 development: Perspectives for future research. Dev. Biol. *476*, 41–52.
1094 https://doi.org/10.1016/j.ydbio.2021.03.005.

1095 27. Behnia, R., and Desplan, C. (2015). Visual circuits in flies: beginning to see the whole
1096 picture. Curr. Opin. Neurobiol. *34*, 125–132.
1097 https://doi.org/10.1016/j.conb.2015.03.010.

1098 28. Ribeiro, I.M.A., Drews, M., Bahl, A., Machacek, C., Borst, A., and Dickson, B.J. (2018).
1099 Visual projection neurons mediating directed courtship in *Drosophila*. Cell *174*, 607-
1100 621.e18. https://doi.org/10.1016/j.cell.2018.06.020.

1101 29. Hindmarsh Sten, T., Li, R., Otopalik, A., and Ruta, V. (2021). Sexual arousal gates visual
1102 processing during *Drosophila* courtship. Nature *595*, 549–553. https://doi.org/10.1038/
1103 s41586-021-03714-w.

1104 30. Joesch, M., Schnell, B., Raghu, S.V., Reiff, D.F., and Borst, A. (2010). ON and OFF
1105 pathways in *Drosophila* motion vision. Nature *468*, 300–304.
1106 https://doi.org/10.1038/nature09545.

1107 31. Strother, J.A., Nern, A., and Reiser, M.B. (2014). Direct observation of ON and OFF
1108 pathways in the *Drosophila* visual system. Curr. Biol. *24*, 976–983. https://doi.org/
1109 10.1016/j.cub.2014.03.017.

1110 32. Fisher, Y.E., Silies, M., and Clandinin, T.R. (2015). Orientation selectivity sharpens motion
1111 detection in *Drosophila*. Neuron *88*, 390–402. https://doi.org/10.1016/j.neuron.2015.
1112 09.033.

1113 33. Maisak, M.S., Haag, J., Ammer, G., Serbe, E., Meier, M., Leonhardt, A., Schilling, T., Bahl,
1114 A., Rubin, G.M., Nern, A., et al. (2013). A directional tuning map of *Drosophila*
1115 elementary motion detectors. Nature *500*, 212–216.
1116 https://doi.org/10.1038/nature12320.

1117 34. Fischbach, K.-F., and Dittrich, A.P.M. (1989). The optic lobe of *Drosophila melanogaster*.
1118 I. A Golgi analysis of wild-type structure. Cell Tissue Res. *258*. https://doi.org/
1119 10.1007/BF00218858.

1120 35. Pinto-Teixeira, F., Koo, C., Rossi, A.M., Neriec, N., Bertet, C., Li, X., Del-Valle-Rodriguez,
1121 A., and Desplan, C. (2018). Development of concurrent retinotopic maps in the fly
1122 motion detection circuit. Cell *173*, 485-498.e11.
1123 https://doi.org/10.1016/j.cell.2018.02.053.

1124 36. Apitz, H., and Salecker, I. (2018). Spatio-temporal relays control layer identity of
1125 direction-selective neuron subtypes in *Drosophila*. Nat. Commun. *9*, 2295.
1126 https://doi.org/10.1038 /s41467-018-04592-z.

1127 37. Takemura, S.-Y., Nern, A., Chklovskii, D.B., Scheffer, L.K., Rubin, G.M., and
1128 Meinertzhagen, I.A. (2017). The comprehensive connectome of a neural substrate for
1129 "ON" motion detection in *Drosophila*. eLife *6*, e24394.
1130 https://doi.org/10.7554/eLife.24394.

1131 38. Shinomiya, K., Takemura, S., Rivlin, P.K., Plaza, S.M., Scheffer, L.K., and Meinertzhagen,
1132 I.A. (2015). A common evolutionary origin for the ON- and OFF-edge motion detection
1133 pathways of the *Drosophila* visual system. Front. Neural Circuits *9*. https://doi.org/
1134 10.3389/fncir.2015.00033.

1135 39. Shinomiya, K., Huang, G., Lu, Z., Parag, T., Xu, C.S., Aniceto, R., Ansari, N., Cheatham, N.,
1136 Lauchie, S., Neace, E., et al. (2019). Comparisons between the ON- and OFF-edge motion
1137 pathways in the *Drosophila* brain. eLife *8*, e40025. https://doi.org/10.7554/eLife.40025.

1138 40. Takemura, S., Bharioke, A., Lu, Z., Nern, A., Vitaladevuni, S., Rivlin, P.K., Katz, W.T.,
1139 Olbris, D.J., Plaza, S.M., Winston, P., et al. (2013). A visual motion detection circuit
1140 suggested by *Drosophila* connectomics. Nature *500*, 175–181.
1141 https://doi.org/10.1038/nature12450.

1142 41. Meier, M., and Borst, A. (2019). Extreme compartmentalization in a *Drosophila* amacrine
1143 cell. Curr. Biol. *29*, 1545-1550.e2. https://doi.org/10.1016/j.cub.2019.03.070.

1144 42. Davis, F.P., Nern, A., Picard, S., Reiser, M.B., Rubin, G.M., Eddy, S.R., and Henry, G.L.
1145 (2020). A genetic, genomic, and computational resource for exploring neural circuit
1146 function. eLife *9*, e50901. https://doi.org/10.7554/eLife.50901.

1147 43. Behnia, R., Clark, D.A., Carter, A.G., Clandinin, T.R., and Desplan, C. (2014). Processing
1148 properties of ON and OFF pathways for *Drosophila* motion detection. Nature *512*, 427–
1149 430. https://doi.org/10.1038/nature13427.

1150 44. Groschner, L.N., Malis, J.G., Zuidinga, B., and Borst, A. (2022). A biophysical account of
1151 multiplication by a single neuron. Nature *603*, 119–123.
1152 https://doi.org/10.1038/s41586-022-04428-3.

1153 45. Takemura, S., Karuppudurai, T., Ting, C.-Y., Lu, Z., Lee, C.-H., and Meinertzhagen, I.A.
1154 (2011). Cholinergic circuits integrate neighboring visual signals in a *Drosophila* motion
1155 detection pathway. Curr. Biol. CB *21*, 2077–2084. https://doi.org/10.1016/j.cub.2011.
1156 10.053.

1157 46. Serbe, E., Meier, M., Leonhardt, A., and Borst, A. (2016). Comprehensive
1158 characterization of the major presynaptic elements to the *Drosophila* OFF motion
1159 detector. Neuron *89*, 829–841. https://doi.org/10.1016/j.neuron.2016.01.006.

1160 47. Meier, M., Serbe, E., Maisak, M.S., Haag, J., Dickson, B.J., and Borst, A. (2014). Neural
1161 circuit components of the *Drosophila* OFF motion vision pathway. Curr. Biol. *24*, 385–
1162 392. https://doi.org/10.1016/j.cub.2014.01.006.

1163 48. Shinomiya, K., Karuppudurai, T., Lin, T.-Y., Lu, Z., Lee, C.-H., and Meinertzhagen, I.A.
1164 (2014). Candidate neural substrates for OFF-edge motion detection in *Drosophila*. Curr.
1165 Biol. *24*, 1062–1070. https://doi.org/10.1016/j.cub.2014.03.051.

1166 49. Braun, A., Borst, A., and Meier, M. (2023). Disynaptic inhibition shapes tuning of OFF-
1167 motion detectors in *Drosophila*. Curr. Biol. CB *33*, 2260-2269.e4. https://doi.org/10.1016
1168 /j.cub.2023.05.007.

1169 50. Borst, A. (2018). A biophysical mechanism for preferred direction enhancement in fly
1170 motion vision. PLOS Comput. Biol. *14*, e1006240. https://doi.org/10.1371/journal.
1171 pcbi.1006240.

1172 51. Haag, J., Arenz, A., Serbe, E., Gabbiani, F., and Borst, A. (2016). Complementary
1173 mechanisms create direction selectivity in the fly. eLife *5*, e17421. https://doi.org
1174 /10.7554/eLife.17421.

1175 52. Haag, J., Mishra, A., and Borst, A. (2017). A common directional tuning mechanism of
1176 *Drosophila* motion-sensing neurons in the ON and in the OFF pathway. eLife *6*, e29044.
1177 https://doi.org/10.7554/eLife.29044.

1178 53. Arenz, A., Drews, M.S., Richter, F.G., Ammer, G., and Borst, A. (2017). The temporal
1179 tuning of the *Drosophila* motion detectors Is determined by the dynamics of their input
1180 elements. Curr. Biol. *27*, 929–944. https://doi.org/10.1016/j.cub.2017.01.051.

1181 54. Hoermann, N., Schilling, T., Haji Ali, A., Serbe, E., Mayer, C., Borst, A., and Pujol-Martí, J.
1182 (2020). A combinatorial code of transcription factors specifies subtypes of visual motion-
1183 sensing neurons in *Drosophila*. Development, dev.186296. https://doi.org/10.1242
1184 /dev.186296.

1185 55. Özel, M.N., Simon, F., Jafari, S., Holguera, I., Chen, Y.-C., Benhra, N., El-Danaf, R.N.,
1186 Kapuralin, K., Malin, J.A., Konstantinides, N., et al. (2021). Neuronal diversity and
1187 convergence in a visual system developmental atlas. Nature *589*, 88–95.
1188 https://doi.org/10.1038/s41586-020-2879-3.

1189 56. Sanfilippo, P., Kim, A.J., Bhukel, A., Yoo, J., Mirshahidi, P.S., Pandey, V., Bevir, H., Yuen,
1190 A., Mirshahidi, P.S., Guo, P., et al. (2024). Mapping of multiple neurotransmitter
1191 receptor subtypes and distinct protein complexes to the connectome. Neuron *112*, 942-
1192 958.e13. https://doi.org/10.1016/j.neuron.2023.12.014.

1193 57. Fendl, S., Vieira, R.M., and Borst, A. (2020). Conditional protein tagging methods reveal
1194 highly specific subcellular distribution of ion channels in motion-sensing neurons. eLife
1195 *9*, e62953. https://doi.org/10.7554/eLife.62953.

1196 58. Kondo, S., Takahashi, T., Yamagata, N., Imanishi, Y., Katow, H., Hiramatsu, S., Lynn, K.,
1197 Abe, A., Kumaraswamy, A., and Tanimoto, H. (2020). Neurochemical organization of the
1198 *Drosophila* brain visualized by endogenously tagged neurotransmitter receptors. Cell
1199 Rep. *30*, 284-297.e5. https://doi.org/10.1016/j.celrep.2019.12.018.

1200 59. Zheng, Z., Lauritzen, J.S., Perlman, E., Robinson, C.G., Nichols, M., Milkie, D., Torrens, O.,
1201 Price, J., Fisher, C.B., Sharifi, N., et al. (2018). A complete electron microscopy volume of
1202 the brain of adult *Drosophila melanogaste*r. Cell *174*, 730-743.e22. https://doi.org/
1203 10.1016/j.cell.2018.06.019.

1204 60. Dorkenwald, S., McKellar, C.E., Macrina, T., Kemnitz, N., Lee, K., Lu, R., Wu, J., Popovych,
1205 S., Mitchell, E., Nehoran, B., et al. (2022). FlyWire: online community for whole-brain
1206 connectomics. Nat. Methods *19*, 119–128. https://doi.org/10.1038/s41592-021-01330-
1207 0.

1208 61. Dorkenwald, S., Matsliah, A., Sterling, A.R., Schlegel, P., Yu, S., McKellar, C.E., Lin, A.,
1209 Costa, M., Eichler, K., Yin, Y., et al. (2023). Neuronal wiring diagram of an adult brain.
1210 Preprint, https://doi.org/10.1101/2023.06.27.546656.

1211 62. Jenett, A., Rubin, G.M., Ngo, T.-T.B., Shepherd, D., Murphy, C., Dionne, H., Pfeiffer, B.D.,
1212 Cavallaro, A., Hall, D., Jeter, J., et al. (2012). A GAL4-driver line resource for *Drosophila*
1213 neurobiology. Cell Rep. *2*, 991–1001. https://doi.org/10.1016/j.celrep.2012.09.011.

1214 63. Tirian, L., and Dickson, B.J. (2017). The VT GAL4, LexA, and split-GAL4 driver line
1215 collections for targeted expression in the *Drosophila* nervous system. Preprint,
1216 https://doi.org/10.1101/198648 https://doi.org/10.1101/198648.

1217 64. Nern, A., Pfeiffer, B.D., Svoboda, K., and Rubin, G.M. (2011). Multiple new site-specific
1218 recombinases for use in manipulating animal genomes. Proc. Natl. Acad. Sci. *108*,
1219 14198–14203. https://doi.org/10.1073/pnas.1111704108.

1220 65. Diegelmann, S., Bate, M., and Landgraf, M. (2008). Gateway cloning vectors for the
1221 LexA-based binary expression system in *Drosophila*. Fly (Austin) *2*, 236–239.
1222 https://doi.org/10.4161/fly.6817.

1223 66. Wagh, D.A., Rasse, T.M., Asan, E., Hofbauer, A., Schwenkert, I., Dürrbeck, H., Buchner, S.,
1224 Dabauvalle, M.-C., Schmidt, M., Qin, G., et al. (2006). Bruchpilot, a protein with
1225 homology to ELKS/CAST, is required for structural integrity and function of synaptic
1226 active zones in *Drosophila*. Neuron *49*, 833–844.
1227 https://doi.org/10.1016/j.neuron.2006.02.008.

1228 67. Mosca, T.J., and Luo, L. (2014). Synaptic organization of the *Drosophila* antennal lobe
1229 and its regulation by the teneurins. eLife *3*, e03726.
1230 https://doi.org/10.7554/eLife.03726.

1231 68. Schmid, A., Hallermann, S., Kittel, R.J., Khorramshahi, O., Frölich, A.M.J., Quentin, C.,
1232 Rasse, T.M., Mertel, S., Heckmann, M., and Sigrist, S.J. (2008). Activity-dependent site-
1233 specific changes of glutamate receptor composition *in vivo*. Nat. Neurosci. *11*, 659–666.
1234 https://doi.org/10.1038/nn.2122.

1235 69. Christiansen, F., Zube, C., Andlauer, T.F.M., Wichmann, C., Fouquet, W., Owald, D.,
1236 Mertel, S., Leiss, F., Tavosanis, G., Farca Luna, A.J., et al. (2011). Presynapses in kenyon
1237 cell dendrites in the mushroom body calyx of *Drosophila*. J. Neurosci. *31*, 9696–9707.
1238 https://doi.org/10.1523/JNEUROSCI.6542-10.2011.

1239 70. Feinberg, E.H., VanHoven, M.K., Bendesky, A., Wang, G., Fetter, R.D., Shen, K., and
1240 Bargmann, C.I. (2008). GFP reconstitution across synaptic partners (GRASP) defines cell
1241 contacts and synapses in living nervous systems. Neuron *57*, 353–363.
1242 https://doi.org/10.1016/j.neuron.2007.11.030.

1243 71. Shearin, H.K., Quinn, C.D., Mackin, R.D., Macdonald, I.S., and Stowers, R.S. (2018). t-
1244 GRASP, a targeted GRASP for assessing neuronal connectivity. J. Neurosci. Methods *306*,
1245 94–102. https://doi.org/10.1016/j.jneumeth.2018.05.014.

1246 72. Macpherson, L.J., Zaharieva, E.E., Kearney, P.J., Alpert, M.H., Lin, T.-Y., Turan, Z., Lee, C.-
1247 H., and Gallio, M. (2015). Dynamic labelling of neural connections in multiple colours by
1248 trans-synaptic fluorescence complementation. Nat. Commun. *6*, 10024. https://doi.org/
1249 10.1038/ncomms10024.

1250 73. Berger-Müller, S., Sugie, A., Takahashi, F., Tavosanis, G., Hakeda-Suzuki, S., and Suzuki, T.
1251 (2013). Assessing the role of cell-surface molecules in central synaptogenesis in the
1252 *Drosophila* visual system. PLoS ONE *8*, e83732. https://doi.org/10.1371/journal.
1253 pone.0083732.

1254 74. Owald, D., Fouquet, W., Schmidt, M., Wichmann, C., Mertel, S., Depner, H., Christiansen,
1255 F., Zube, C., Quentin, C., Körner, J., et al. (2010). A Syd-1 homologue regulates pre- and
1256 postsynaptic maturation in *Drosophila*. J. Cell Biol. *188*, 565–579.
1257 https://doi.org/10.1083 /jcb.200908055.

1258 75. Buhmann, J., Sheridan, A., Malin-Mayor, C., Schlegel, P., Gerhard, S., Kazimiers, T.,
1259 Krause, R., Nguyen, T.M., Heinrich, L., Lee, W.-C.A., et al. (2021). Automatic detection of
1260 synaptic partners in a whole-brain *Drosophila* electron microscopy data set. Nat.
1261 Methods *18*, 771–774. https://doi.org/10.1038/s41592-021-01183-7.

1262 76. Heinrich, L., Funke, J., Pape, C., Nunez-Iglesias, J., and Saalfeld, S. (2018). Synaptic cleft
1263 segmentation in non-isotropic volume electron microscopy of the complete *Drosophila*
1264 brain. Preprint at arXiv, https://doi.org/10.48550/ARXIV.1805.02718.

1265 77. Götz, K.G. (1968). Flight control in *Drosophila* by visual perception of motion. Kybernetik
1266 *4*, 199–208. https://doi.org/10.1007/BF00272517.

1267 78. Mauss, A.S., and Borst, A. (2020). Optic flow-based course control in insects. Curr. Opin.
1268 Neurobiol. *60*, 21–27. https://doi.org/10.1016/j.conb.2019.10.007.

1269 79. Ryu, L., Kim, S.Y., and Kim, A.J. (2022). From photons to behaviors: Neural
1270 implementations of visual behaviors in *Drosophila*. Front. Neurosci. *16*, 883640.
1271 https://doi.org/10.3389/fnins.2022.883640.

1272 80. Leonte, M.-B., Leonhardt, A., Borst, A., and Mauss, A.S. (2021). Aerial course
1273 stabilization is impaired in motion-blind flies. J. Exp. Biol. *224*, jeb242219.
1274 https://doi.org/10.1242 /jeb.242219.

1275 81. Bahl, A., Ammer, G., Schilling, T., and Borst, A. (2013). Object tracking in motion-blind
1276 flies. Nat. Neurosci. *16*, 730–738. https://doi.org/10.1038/nn.3386.

1277 82. Schnell, B., Raghu, S.V., Nern, A., and Borst, A. (2012). Columnar cells necessary for
1278 motion responses of wide-field visual interneurons in *Drosophila*. J. Comp. Physiol. A
1279 *198*, 389–395. https://doi.org/10.1007/s00359-012-0716-3.

1280 83. Schilling, T., and Borst, A. (2015). Local motion detectors are required for the
1281 computation of expansion flow-fields. Biol. Open *4*, 1105–1108.
1282 https://doi.org/10.1242/bio.012690.

1283 84. Ni, J.-Q., Liu, L.-P., Binari, R., Hardy, R., Shim, H.-S., Cavallaro, A., Booker, M., Pfeiffer,
1284 B.D., Markstein, M., Wang, H., et al. (2009). A Drosophila resource of transgenic RNAi
1285 lines for neurogenetics. Genetics *182*, 1089–1100.
1286 https://doi.org/10.1534/genetics.109.103630.

1287 85. Ni, J.-Q., Zhou, R., Czech, B., Liu, L.-P., Holderbaum, L., Yang-Zhou, D., Shim, H.-S., Tao,
1288 R., Handler, D., Karpowicz, P., et al. (2011). A genome-scale shRNA resource for
1289 transgenic RNAi in *Drosophila*. Nat. Methods *8*, 405–407.
1290 https://doi.org/10.1038/nmeth.1592.

1291 86. Schilling, T., Ali, A.H., Leonhardt, A., Borst, A., and Pujol-Martí, J. (2019). Transcriptional
1292 control of morphological properties of direction-selective T4/T5 neurons in *Drosophila*.
1293 Development, dev.169763. https://doi.org/10.1242/dev.169763.

1294 87. Shinomiya, K., Nern, A., Meinertzhagen, I.A., Plaza, S.M., and Reiser, M.B. (2022).
1295 Neuronal circuits integrating visual motion information in *Drosophila melanogaster.*
1296 Curr. Biol. CB *32*, 3529-3544.e2. https://doi.org/10.1016/j.cub.2022.06.061.

1297 88. Albuquerque, E.X., Pereira, E.F.R., Alkondon, M., and Rogers, S.W. (2009). Mammalian
1298 nicotinic acetylcholine receptors: from structure to function. Physiol. Rev. *89*, 73–120.
1299 https://doi.org/10.1152/physrev.00015.2008.

1300 89. Abrams, P., Andersson, K.-E., Buccafusco, J.J., Chapple, C., de Groat, W.C., Fryer, A.D.,
1301 Kay, G., Laties, A., Nathanson, N.M., Pasricha, P.J., et al. (2006). Muscarinic receptors:
1302 their distribution and function in body systems, and the implications for treating
1303 overactive bladder. Br. J. Pharmacol. *148*, 565–578.
1304 https://doi.org/10.1038/sj.bjp.0706780.

1305 90. Schuster, R., Phannavong, B., Schröder, C., and Gundelfinger, E.D. (1993).
1306 Immunohistochemical localization of a ligand-binding and a structural subunit of
1307 nicotinic acetylcholine receptors in the central nervous system of *Drosophila*
1308 *melanogaster*. J. Comp. Neurol. *335*, 149–162. https://doi.org/10.1002/cne.903350202.

1309 91. Gundelfinger, E.D. (1992). How complex is the nicotinic receptor system of insects?
1310 Trends Neurosci. *15*, 206–211. https://doi.org/10.1016/0166-2236(92)90035-7.

1311 92. Jonas, P.E., Phannavong, B., Schuster, R., Schröder, C., and Gundelfinger, E.D. (1994).
1312 Expression of the ligand-binding nicotinic acetylcholine receptor subunit Dα2 in the
1313 *Drosophila* central nervous system. J. Neurobiol. *25*, 1494–1508.
1314 https://doi.org/10.1002/ neu.480251203.

1315 93. Thany, S.H. (2010). Electrophysiological studies and pharmacological properties of insect
1316 native nicotinic acetylcholine receptors. In Insect Nicotinic Acetylcholine Receptors
1317 Advances in Experimental Medicine and Biology., S. H. Thany, ed. (Springer New York),
1318 pp. 53–63. https://doi.org/10.1007/978-1-4419-6445-8_5.

1319 94. Chamaon, K., Schulz, R., Smalla, K.-H., Seidel, B., and Gundelfinger, E.D. (2000). Neuronal
1320 nicotinic acetylcholine receptors of *Drosophila melanogaster*: the α-subunit Dα3 and
1321 the β-type subunit ARD co-assemble within the same receptor complex. FEBS Lett. *482*,
1322 189–192. https://doi.org/10.1016/S0014-5793(00)02057-3.

1323 95. Chamaon, K., Smalla, K., Thomas, U., and Gundelfinger, E.D. (2002). Nicotinic
1324 acetylcholine receptors of *Drosophila*: three subunits encoded by genomically linked

genes can co-assemble into the same receptor complex. J. Neurochem. *80*, 149–157. https://doi.org/10.1046/j.0022-3042.2001.00685.x.

96. Deng, B., Li, Q., Liu, X., Cao, Y., Li, B., Qian, Y., Xu, R., Mao, R., Zhou, E., Zhang, W., et al. (2019). Chemoconnectomics: mapping chemical transmission in *Drosophila*. Neuron *101*, 876-893.e4. https://doi.org/10.1016/j.neuron.2019.01.045.

97. Bahl, A., Serbe, E., Meier, M., Ammer, G., and Borst, A. (2015). Neural mechanisms for *Drosophila* contrast vision. Neuron *88*, 1240–1252. https://doi.org/10.1016/j.neuron.2015.11.004.

98. Namiki, S., Dickinson, M.H., Wong, A.M., Korff, W., and Card, G.M. (2018). The functional organization of descending sensory-motor pathways in *Drosophila*. eLife *7*, e34272. https://doi.org/10.7554/eLife.34272.

99. Komori, Y., Takayama, K., Okamoto, N., Kamiya, M., Koizumi, W., Ihara, M., Misawa, D., Kamiya, K., Yoshinari, Y., Seike, K., et al. (2023). Functional impact of subunit composition and compensation on *Drosophila melanogaster* nicotinic receptors-targets of neonicotinoids. PLoS Genet. *19*, e1010522. https://doi.org/10.1371/journal.pgen.1010522.

100. Pfeiffer, B.D., Ngo, T.-T.B., Hibbard, K.L., Murphy, C., Jenett, A., Truman, J.W., and Rubin, G.M. (2010). Refinement of tools for targeted gene expression in *Drosophila*. Genetics *186*, 735–755. https://doi.org/10.1534/genetics.110.119917.

101. Raccuglia, D., Huang, S., Ender, A., Heim, M.-M., Laber, D., Suárez-Grimalt, R., Liotta, A., Sigrist, S.J., Geiger, J.R.P., and Owald, D. (2019). Network-specific synchronization of electrical slow-wave oscillations regulates sleep drive in *Drosophila*. Curr. Biol. CB *29*, 3611-3621.e3. https://doi.org/10.1016/j.cub.2019.08.070.

102. Jin, X., Tian, Y., Zhang, Z.C., Gu, P., Liu, C., and Han, J. (2021). A subset of DN1p neurons integrates thermosensory inputs to promote wakefulness via CNMa signaling. Curr. Biol. CB *31*, 2075-2087.e6. https://doi.org/10.1016/j.cub.2021.02.048.

103. Schindelin, J., Arganda-Carreras, I., Frise, E., Kaynig, V., Longair, M., Pietzsch, T., Preibisch, S., Rueden, C., Saalfeld, S., Schmid, B., et al. (2012). Fiji: an open-source platform for biological-image analysis. Nat. Methods *9*, 676–682. https://doi.org/10.1038/ nmeth.2019.

104. Buchner, E. (1976). Elementary movement detectors in an insect visual system. Biol. Cybern. *24*, 85–101. https://doi.org/10.1007/BF00360648.

105. Seelig, J.D., Chiappe, M.E., Lott, G.K., Dutta, A., Osborne, J.E., Reiser, M.B., and Jayaraman, V. (2010). Two-photon calcium imaging from head-fixed *Drosophila* during optomotor walking behavior. Nat. Methods *7*, 535–540. https://doi.org/10.1038/nmeth.1468.

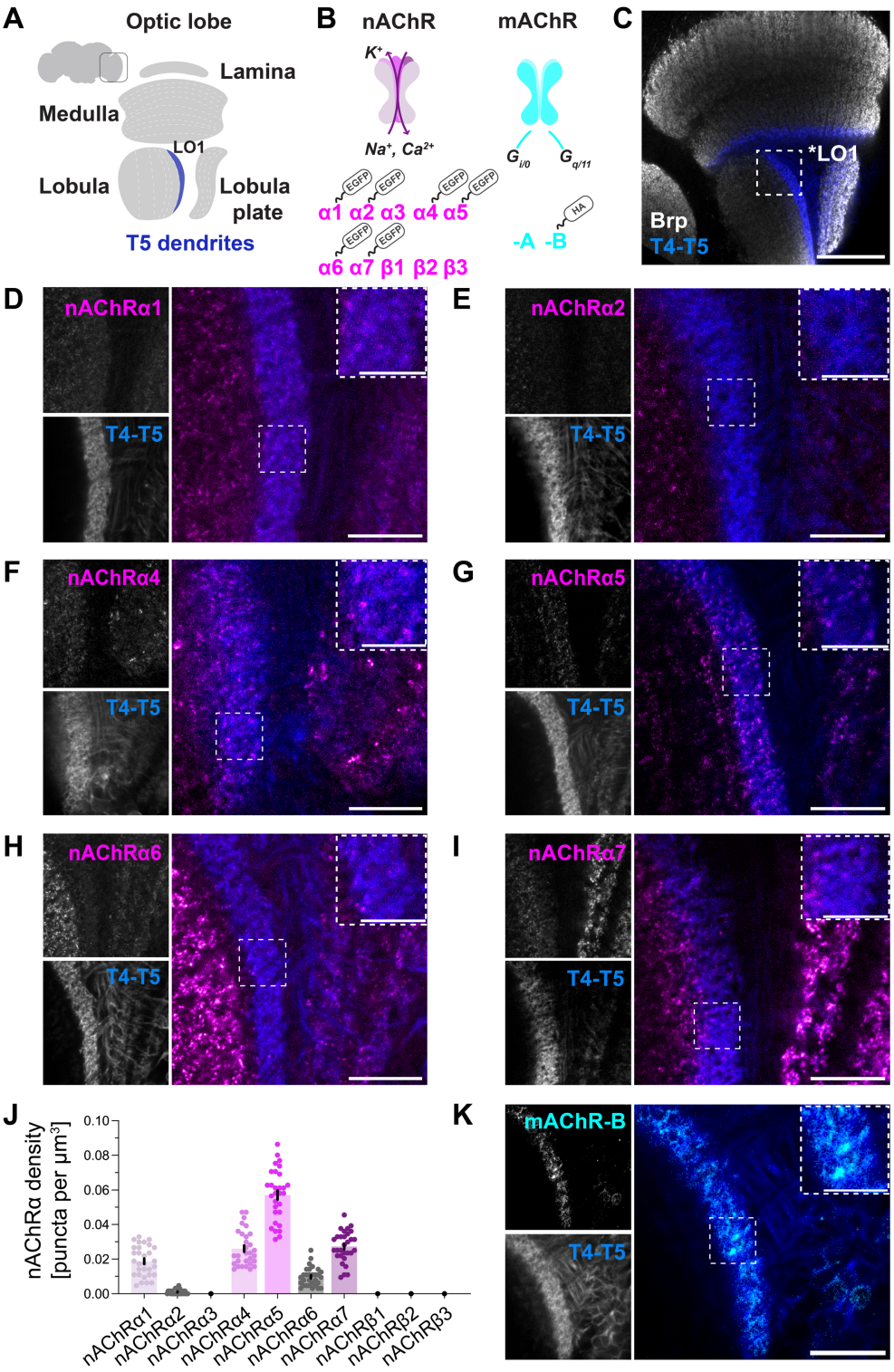

Figure 1. AChR expression on T5 dendrites

(A) Schematic representation of T5 dendrites residing in lobula layer 1 (LO1) of the *Drosophila* optic lobe (OL).

(B) Schematic representation of nicotinic ionotropic (magenta) and muscarinic metabotropic AChRs (cyan) in *Drosophila*. Out of the seven nAChRα subunits, six were tagged with EGFP[22]. The mAChR-B was tagged with the HA peptide tag (C.H.Lee)

(C) OL (grey) with T4 and T5 dendrites (R42F06-Gal4>UAS-myr::tdTomato, blue) in M10 and LO1 accordingly. Scale bar 40µm.

(D-I) nAChRα1, nAChRα2, nAChRα4, nAChRα5, nAChRα6 and nAChRα7 (nAChRα::EGFP, magenta) subunit expression on T5 dendrites (R42F06-Gal4>UAS-myr::tdTomato, blue). Scale bar 10µm, inset 5µm.
(J) Density of nAChRα subunit expression on T5 dendrites across 30 ROIs in LO1 (optic lobes n=6). nAChRα3, nAChRβ1, nAChRβ2 and nAChRβ3 subunits were not addressed. Subunits with the lowest expression levels are in grey. Data is mean ± SEM.
(K) Overexpression of mAChR-B (UAS-mAChR-B::HA, cyan) on T5 dendrites (R42F06-Gal4>UAS-myr::tdTomato, blue). Scale bar 10µm, inset 5µm.

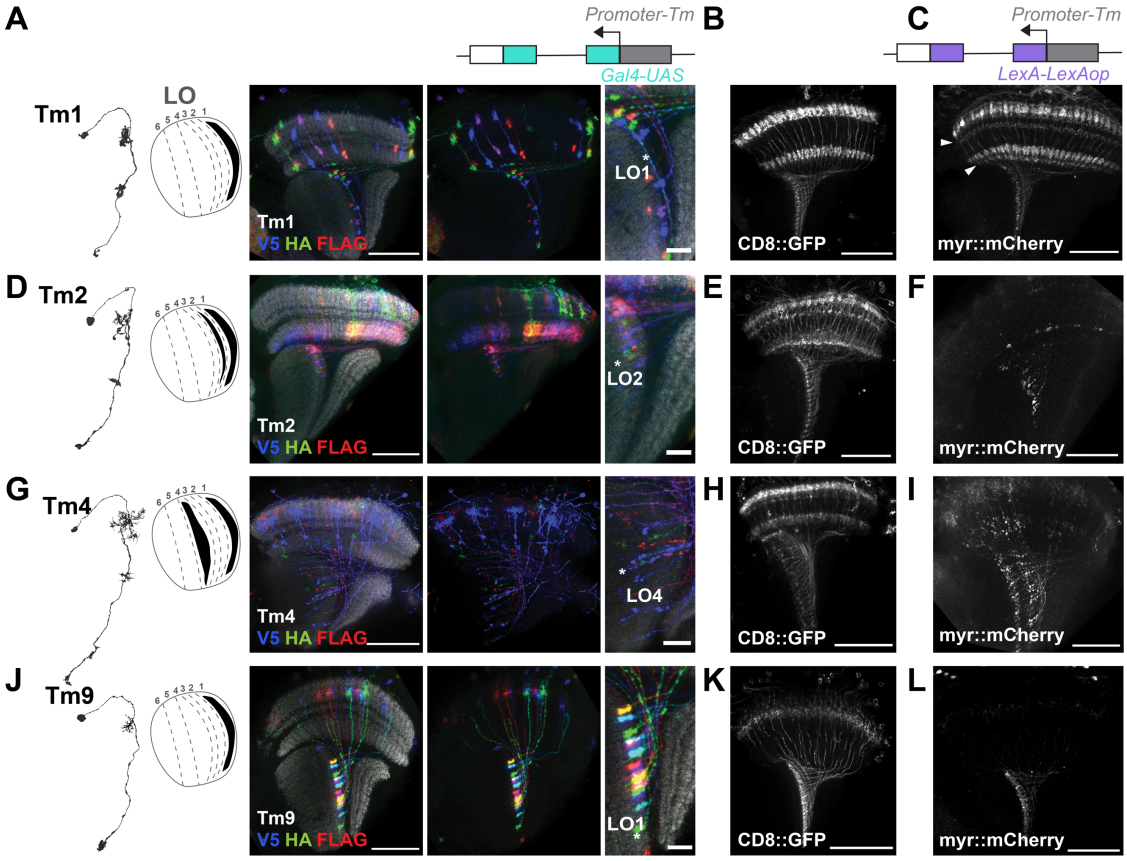

Figure 2. Morphological identification of the four columnar T5 cholinergic input neurons

(A) Electron microscopy (EM)(flywire.ai) reconstruction of a Tm1 neuron reveals two loci of arborization in medulla. Schematic representation of the Tm1 axonal terminal localization in LO1. Tm1-Gal4 expression (cyan) of the MultiColor FlpOut cassette (V5, HA, FLAG) and axonal localization in LO. Scale bar 40µm and 10µm.

(B) Whole population labelling of Tm1 neurons (R74G01-Gal4>UAS-CD8::GFP). Scale bar 40µm.

(C) Whole population labelling of Tm1-LexA (purple) neurons (VT041034-LexAGAD>LexAop-myr::mCherry). Arrows represent additional dendritic ramifications that lack in (B). Scale bar 40µm.

(D-F) As in (A-C), but for Tm2 neurons (VT012282-Gal4, VT058650-LexAGAD).

(G-I) As in (A-C), but for Tm4 neurons (R35H01-Gal4, R53C02-LexAGAD).

(J-L) As in (A-C), but for Tm9 neurons (VT065303-Gal4, R24C08-LexAp65).

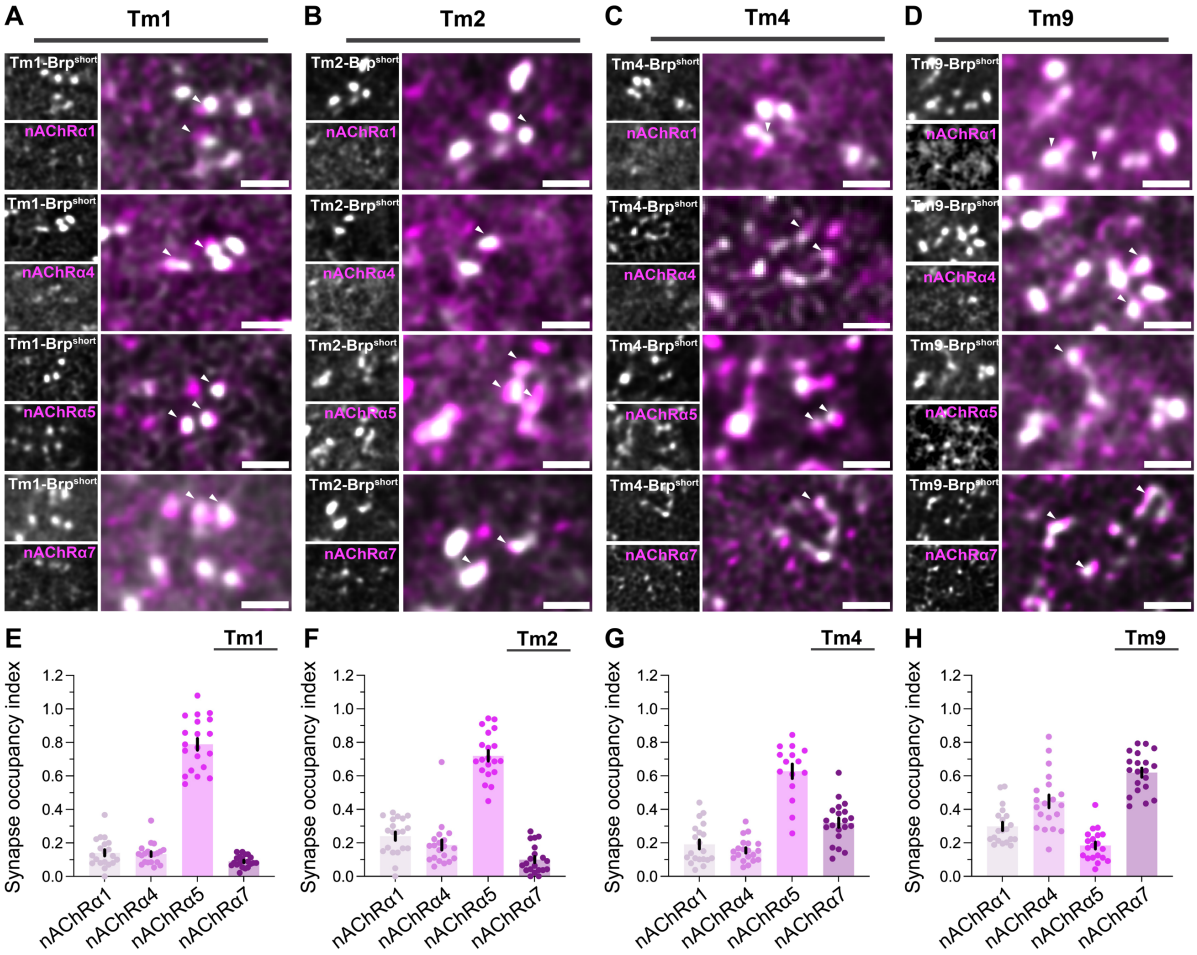

Figure 3. Differential synaptic localization of nAChRα subunits in Tm synapses
(A-D) Trans-synaptic alignment of Tm1, Tm2, Tm4 and Tm9 boutons (Tm-Gal4> UAS-Brp$^{short::mStraw}$, grey) with the nAChRα1, nAChRα4, nAChRα5 and nAChRα7 subunits (nAChRα::EGFP, magenta) in LO1. Arrows indicate the Brp$^{short::mStraw}$-receptor punctum trans-synaptic alignment. Scale bar 1µm. (E-H) Synapse occupancy of Tm1, Tm2, Tm4 and Tm9 boutons with nAChRα1 (pale magenta), nAChRα4 (light magenta), nAChRα5 (magenta) and nAChRα7 (dark magenta) subunits in LO1 (optic lobes n=4, ROIs N=20, for Tm4-nAChRα5 n=3, N=15). Data is mean ± SEM.

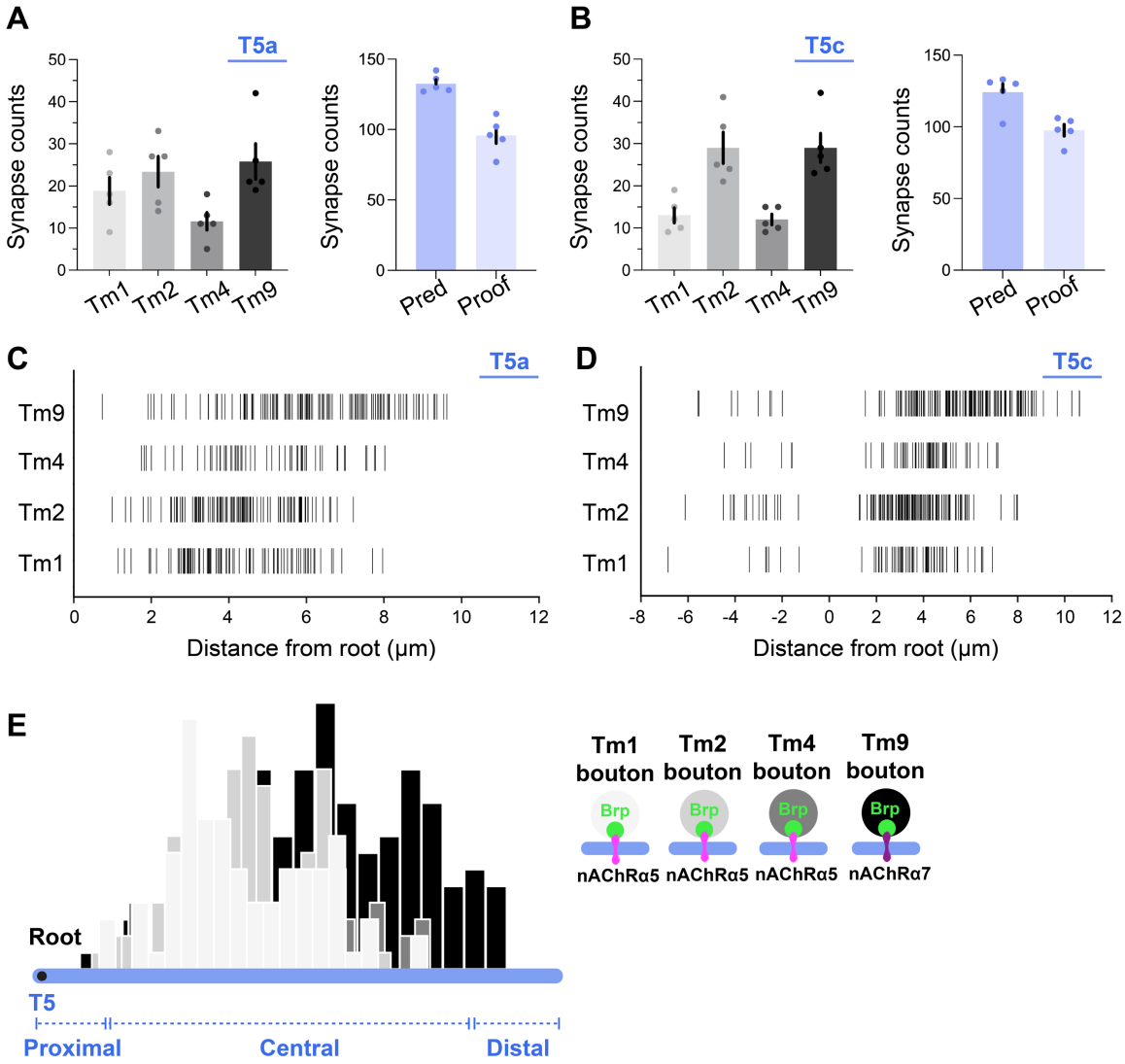

Figure 4. Wiring of Tm1, Tm2, Tm4 and Tm9 on T5 dendrites

(A) Counts of Tm1, Tm2, Tm4 and Tm9 synapses in T5a dendrites (T5a cells n=5, flywire.ai) (left). Counts of predicted (n=663) to proofread (n=479) Tm synapses in T5a dendrites (right). Data is mean ± SEM.

(B) As in (A) for T5c dendrites (T5c cells n=5, flywire.ai) (left). Counts of predicted (n=621) to proofread (n=488) Tm synapses in T5c dendrites (right). Data is mean ± SEM.

(C) Dendritic localization of Tm synapses across the T5a anterior-posterior axis (T5a cells n=5). Root is considered the first dendritic branch point.

(D) Dendritic localization of Tm synapses across the T5c dorso-ventral axis (T5c cells n=5).

(E) Schematic representation of Tm-T5a dendritic synapses and the observed postsynaptic receptor heterogeneity in terms of the most abundant nAChR subunit as in Figure 3E-H.

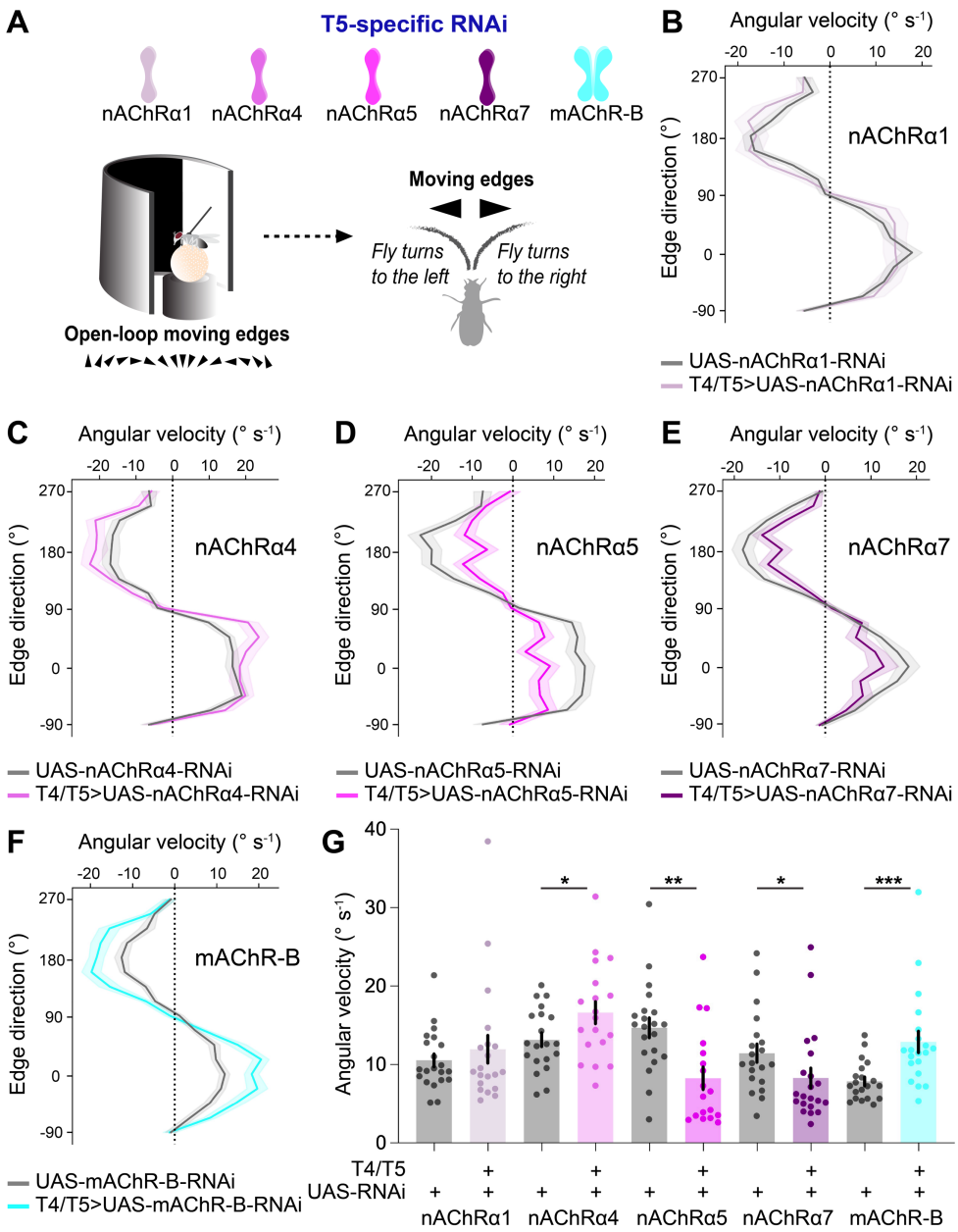

Figure 5. Fly optomotor response post-AChR knock-down

(A) Schematic workflow representation for the behavioral assessment of AChR knock-down flies.

(B) Trajectory (angular velocity) of nAChRα1 knock-down flies (R42F06-p65.AD; VT043070-Gal4.DBD>UAS-nAChRα1-RNAi, pale magenta, flies n=20) while presented to a sequence of upward to rightward to downward to leftward OFF edge motion compared to the parental control flies (UAS-nAChRα1-RNAi, grey n=21). The dark lines represent the mean ± SEM.

(C-F) Same as in (B) for the nAChRα4 (light magenta n=19, grey n=20), nAChRα5 (magenta n=18, grey n=21), nAChRα7 (dark magenta, n=21, grey n=20), mAChR-B (cyan n=20, grey n=20) knock-down flies.

(G) Angular velocity of control and AChR knock-down flies. The normality of distribution was assessed with the use of Shapiro-Wilk test. *p<0.05, **p<0.01, ***p<0.001. Data is mean ± SEM.

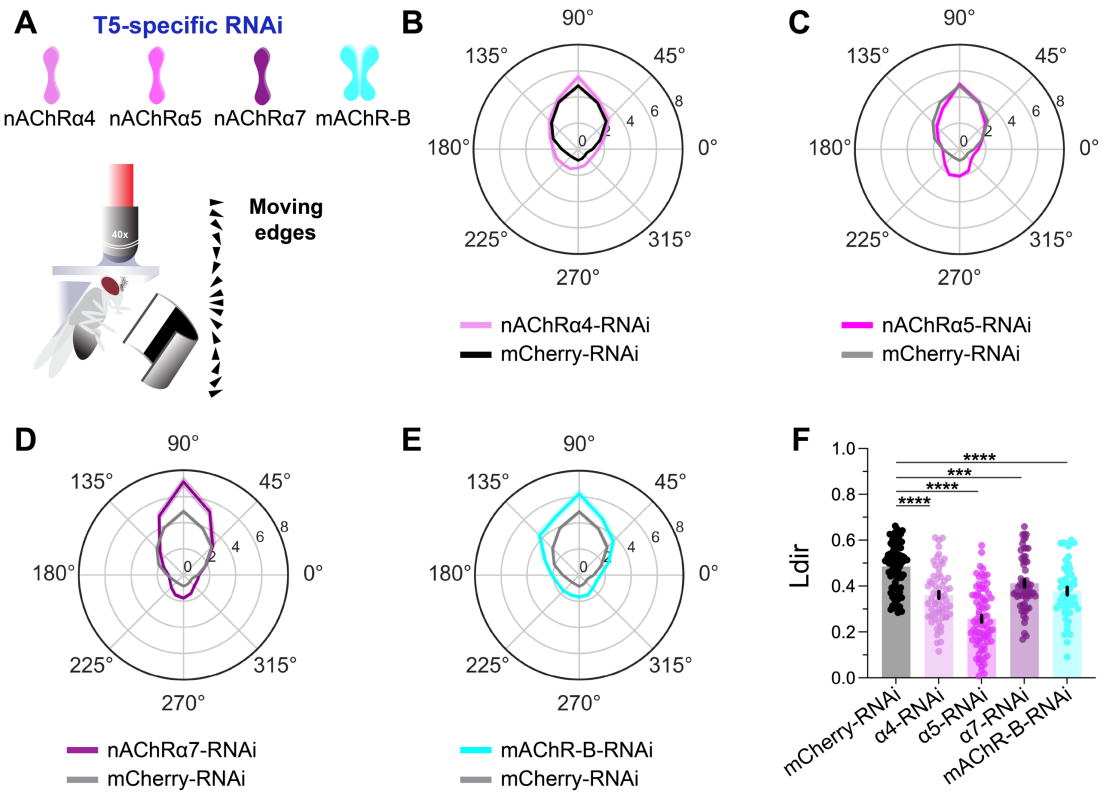

Figure 6. Directional tuning of T5 cells post-AChR knock-down

(A) Schematic workflow representation for the two-photon calcium imaging in AChR knock-down T5 cells.

(B) Polar plot of the maximum responses (ΔF/F) across sixteen OFF edge directions (º) of T5c cells for mCherry controls (black, flies n=7, ROIs N=85, shown as grey in C, D and E) and nAChRα4 RNAi (light magenta, n=7, N=61) conditions (R39H12-Gal4>AChR-RNAi, VT50384-LexA>LexAop-IVS-GCaMP6m). The dark lines represent the mean (68% CI).

(C) Same as in (B) for nAChRα5 RNAi flies (magenta, n=7, N=82).

(D) Same as in (B) for nAChRα7 RNAi flies (dark magenta, n=7, N=60).

(E) Same as in (B) for mAChR-B RNAi flies (cyan, n=7, N=54).

(F) Directional tuning index. N_{ROIs} as in B-E. The normality of distribution was assessed with the use of Shapiro-Wilk test. ***p<0.001, ****p<0.0001. Data is mean ± SEM.